Helios and Juliette: Two falsely acclaimed medicanes?

Leo Pio d'Adderio, Giulia Panegrossi, Stavros Dafis, Jean-Francois Rysman, Daniele Casella, Paolo Sanò, Alessandro Fuccello, Mario Marcello Miglietta

Atmospheric Research 299 (2024) 107179

Contents lists available at ScienceDirect

Atmospheric Research

journal homepage: www.elsevier.com/locate/atmosres

Helios and Juliette: Two falsely acclaimed medicanes?

Leo Pio D'Adderio [a], Giulia Panegrossi [a,*], Stavros Dafis [b,c], Jean-Francois Rysman [d], Daniele Casella [a], Paolo Sanò [a], Alessandro Fuccello [e], Mario Marcello Miglietta [f,g]

[a] National Research Council of Italy, Institute of Atmospheric Sciences and Climate (CNR-ISAC), Rome, Italy
[b] Institute of Environmental Research and Sustainable Development, National Observatory of Athens, Athens, Greece
[c] Data4Risk, Paris, France
[d] LMD & LadHyX, CNRS, École Polytechnique, Institut Polytechnique de Paris, Palaiseau, France
[e] Centro Nazionale di Meteorologia e Climatologia Aerospaziale, CNMCA, Pratica di Mare, Italy
[f] National Research Council of Italy, Institute of Atmospheric Sciences and Climate (CNR-ISAC), Padua, Italy
[g] Department of Earth and Geoenvironmental Sciences, University of Bari, Bari, Italy

ARTICLE INFO

Keywords:
Tropical-like cyclone
Medicane
Remote sensing
Warm core
Microphysics
Synoptic analysis
Passive microwave

ABSTRACT

The present work analyzes the synoptic, thermodynamic, and microphysics characteristics of two Mediterranean cyclones that occurred in February–March 2023. The analysis is mainly carried out through the use of passive microwave (PMW) satellite measurements, which allow us to follow the cyclones' evolution and state whether Helios and Juliette can be considered as Mediterranean tropical-like cyclones (i.e., medicanes). Both cyclones show a very similar evolution, with a low-stratospheric warm air anomaly during the development phase, followed by the development of a warm anomaly in the low−/mid-troposphere. This feature is often observed in medicanes (e.g., Qendresa, Zorbas), except for few cases (i.e., Medicane Ianos, which shows a warm core (WC) development clearly driven by diabatic processes without a preliminary warming signal in the lower stratosphere and upper troposphere). The analysis carried out highlights that, while Helios maintains this setting through its whole lifetime, Juliette undergoes tropical transition in the final stage of its evolution. As opposed to most medicane cases, the PMW precipitation microphysics diagnostics shows the predominance of shallow clouds, with almost total absence of ice hydrometeors and deep convection in the proximity of the WC center (i.e., within 100 km radius) for Helios and during the initial stage of Juliette. PMW radiometry provides strong indication that diabatic heating plays a role in the WC development when the onset of deep convection features is identified in the proximity of the Juliette cyclone center. Moreover, the PMW cloud-top height product does not show a closed cloud-free eye for Helios, while it is observed for the final stage of Juliette as often happens during medicanes' mature phase. Therefore, we deem that while Helios can be labeled as a warm seclusion, Juliette can be included in the tropical-like cyclone category.

1. Introduction

Derived from the merging of "Mediterranean" and "hurricane," Medicanes refer to mesoscale cyclones with occasionally hurricane-like features that develop over the Mediterranean Sea (Emanuel, 2005). Medicanes may cause severe socio-economic (Lagouvardos et al., 2022; Loli et al., 2022) and environmental impacts (Menna et al., 2023) in this densely populated region, and require interdisciplinary approaches to understand their dynamics and improve our ability to forecast their intensity and impacts. Medicanes encompass characteristics of both extratropical and tropical cyclones during their lifetime (D'Adderio et al., 2022; Dafis et al., 2020, 2018; Miglietta et al., 2013). The tropical-like characteristics include a warm core (WC) (driven by diabatic processes), a spirally distributed cloud/rain bands around a front-less cyclone, with deep convection (DC) close to the cyclone center and may include a cloud-free eye. Many so-called Medicanes in the literature resemble the subtropical cyclones that develop in the sub-tropics and mid-latitudes 20°N – 40°N (Bentley et al., 2017; Bentley and Metz, 2016; Evans and Guishard, 2009; González-Alemán et al., 2015) or 20°S – 40°S (Dowdy et al., 2019; Evans and Braun, 2012), where tropical cyclones can also develop.

Recently, a passive microwave (PMW) technique originally developed

* Corresponding author.
E-mail address: g.panegrossi@isac.cnr.it (G. Panegrossi).

https://doi.org/10.1016/j.atmosres.2023.107179
Received 1 August 2023; Received in revised form 11 December 2023; Accepted 11 December 2023
Available online 18 December 2023

for WC detection in Tropical Cyclones (Brueske and Velden, 2003), has been applied to medicanes (Panegrossi et al., 2023). Starting from PMW diagnostics for DC, ice water path (IWP) and cloud-top height (CTH) (Rysman et al., 2021), the authors highlighted the large variability, but also some possible clustering, of both thermodynamic and microphysics structures characterizing several medicanes. Only Medicanes Ianos and Zorbas developed a persistent deep WC structure, extending to the upper troposphere (up to 200 hPa), among six analyzed medicanes, showing similar structures with Tropical Cyclones. The different characteristics of medicanes were also discussed in (Flaounas et al., 2021) from a dynamical point of view, using reanalysis data. Based on the potential vorticity evolution of medicanes, the authors questioned whether these cyclones can be considered as purely diabatic systems, like Tropical Cyclones. This debate can be partly explained by the non-linear interaction of latent heat release with baroclinic dynamics (Kuo et al., 1991), since medicanes develop in baroclinic environments, and by the abrupt land-sea contrast within the Mediterranean Basin (Flaounas et al., 2022). However, confusion remains evident in the use of the term "medicane", both in mass media and in the scientific literature. Currently, the term is used indistinctly to represent subtropical cyclones or warm air seclusions (Fita and Flaounas, 2018; Mazza et al., 2017; Nastos et al., 2018) and cyclones which show visual and physical analogies with tropical cyclones (Miglietta and Rotunno, 2019). Under the framework of the MedCyclones COST Action CA19109 (Hatzaki et al., 2023), a working group of more than 30 scientists (including the authors of this study) seek to provide an official definition of medicanes. In order to contribute to this effort, the present study investigates the lifecycle of two Mediterranean cyclones (Helios and Juliette) that developed at the end of winter 2023 and were classified as medicanes in the mass media and some meteorological service websites. Our work aims to provide a comprehensive description of Helios and Juliette mainly from an observational point of view, in order to compare them with other well-documented cyclones. More specifically, the PMW WC detection technique (Brueske and Velden, 2003; Panegrossi et al., 2023) is used to study the evolution of WC development in Helios and Juliette. In addition, high-frequency PMW channels are used to detect DC and estimate the CTH and IWP, as well as precipitation and cloud property diagnostics are utilized throughout the cyclones' development.

The paper is organized as follows: Section 2 describes the instrumentation and the data used in this work, Section 3 reports a detailed description of the two case studies (i.e., cyclones Helios and Juliette), while the discussion and the conclusions are in Section 4.

2. Instrumentation and data

The PMW measurements from different radiometers in the Global Precipitation Measurement (GPM) mission constellation (Hou et al., 2014; Skofronick-Jackson et al., 2017) are used to provide a comprehensive description of the two case studies analyzed in this work. The GPM Microwave Imager (GMI) and the Advanced Microwave Scanning Radiometer 2 (AMSR2) are used to characterize precipitation microphysics, while the Advanced Microwave Sounding Unit/Microwave Humidity Sounder (AMSU/MHS) and the Advanced Technology Microwave Sounder (ATMS) are used for upper tropospheric air intrusion and WC diagnostics. The Level 1C data, corresponding to the brightness temperature (TB) measured by the microwave (MW) radiometers described in the next subsections, are used in this work. In addition, the DEEPSTORM algorithm (DEEP moiSt aTmospheric cOnvection from micRowave radioMeter - (Rysman et al., 2022, 2021) - based on PMW high-frequency channel measurements) is used to derive the cloud top height (CTH) and Ice Water Path (IWP), while the methodology of (Hong et al., 2005) is used for DC detection.

2.1. Advanced Microwave Scanning Radiometer 2 (AMSR2)

The JAXA's GCOM-W1 AMSR2 (Okuyama and Imaoka, 2015), is a conical scanning radiometer providing measurements over a swath width of about 1450 km at a nominal incidence angle of 55°. It has six channels at frequencies ranging from 6.925 to 89 GHz, all with dual-polarization capabilities (for a total of 12 channels in this frequency range). The AMSR2 sampling interval is 10 km for all the channels, except for the 89 GHz channel (the sampling interval is 5 km). Conversely, the AMSR2 spatial resolution ranges between 3 km × 5 km at 89 GHz and 35 km × 62 km at 6.925 GHz.

2.2. GPM Microwave Imager (GMI)

The GPM Microwave Imager (GMI) onboard the GPM Core Observatory (GPM-CO) is a conical-scanning radiometer (Draper et al., 2015) with a 904 km wide swath and thirteen channels at frequencies ranging between 10 GHz and 190 GHz, ten of them operating in dual-polarization mode. Among the currently operating PMW radiometers, GMI is the most advanced in terms of channel assortment and spatial resolution (4 km × 7 km at frequencies >89 GHz, decreasing to 19 km × 32 km at 10 GHz) and 5 km sampling distance.

2.3. Advanced Microwave Sounding Unit-A (AMSU-A)/Microwave Humidity Sounder (MHS)

Both the AMSU-A and the MHS are cross-track scanning radiometers currently onboard five satellites (NOAA-18/19 and MetOp-A/B/C) and are equipped with 20 sounding and window channels (15 channels for AMSU-A and 5 channels for MHS) over a swath width of about 2200 km. While the AMSU-A is mainly designed for atmospheric temperature sounding (with 12 channels in the 50 GHz band – oxygen absorption band), the MHS, with two window channels at 89 and 150 GHz and three channels in the 183.31 GHz water vapor absorption band, is primarily intended for moisture sounding. Even if they provide data over the same swath, the MHS sampling rate is three times higher than AMSU-A (1.1° with respect to 3.3°, respectively), resulting in different spatial resolution between the two sensors (from about 50 km for AMSU-A to about 16 km for MHS at nadir). As a cross-track swath is used, there is a degradation in resolution from nadir to the edge of the swath. Additional and more detailed information are provided in (Yan and Ahmad, 2021).

2.4. Advanced Technology Microwave Sounder (ATMS)

The ATMS (Weng et al., 2013) is a cross-track scanning microwave radiometer on board the NOAA NPP satellite and JPSS satellites. ATMS has 22 channels, ranging from 23 to 183 GHz, over a 2200 km wide swath providing both temperature sounding (channels 1–16, most of them within the oxygen absorption band) and humidity sounding measurements (channels 17–22, from 89 to 183 GHz). Differently from AMSU-A/MHS, the angular sampling is the same for all channels (1.1°), while the different beam width, depending on the channels considered, provides nadir resolutions of 74.78 (channels 1–2), 31.64 (channels 3–16) and 15.82 km (channels 17–22), respectively. As highlighted for AMSU-A, being also ATMS a cross-track scanning radiometer, the spatial resolution decreases moving toward the edge of the swath (Zou et al., 2013).

3. Case studies

Two cyclones, which occurred in February–March 2023, named Helios and Juliette, are analyzed in this study. Starting from the synoptic characteristics leading to the development of the cyclones, a thermodynamical and microphysical analysis is carried out to investigate the possible tropical-like features for both cyclones.

3.1. Cyclone Helios: 8–10 February 2023

Helios occurred between 8 and 10 February 2023 in the southern Mediterranean Sea affecting Sicily, Malta, Tunisia and Libya. Two

phases in the cyclone lifetime can be identified from the microphysical and the dynamical point of view. During the first phase (mainly 8 and 9 February), Helios showed distinct DC features, produced by the convergence of cold air on the NorthEast and subtropical milder air on the SouthWest side. During the second phase, it attained a more barotropic structure showing visual features similar to tropical cyclones. The images of the EUMETSAT Meteosat Second Generation (MSG) satellite in the SEVIRI Visible (VIS) channels provide a visual characterization of Helios highlighting the transition between the two phases (Fig. 1).

3.1.1. Synoptic analysis

At 00:00 UTC, 8 February 2023, the 500 hPa geopotential height over northern Europe (Fig. 2) is characterized by an extensive ridge extending longitudinally from the British Isles to Siberia. As a result, a northeasterly flow is established in Western Europe; a cold air mass moving on its southern border counterclockwise around a low geopotential height center over Turkey and over the Iberian Peninsula, reaches the central and the western Mediterranean resulting in strong baroclinicity. At low levels, an anticyclone over Eastern Europe conveys very cold air over the Balkans, Italy, and Spain, and interacts with a low-pressure system centered over the western part of the Iberian Peninsula; another pressure minimum is located ahead of the upper-level trough axis, in Algeria mainland.

Twenty-four hours later, the 500 hPa geopotential minimum is located over Corsica and Sardinia, associated with a very cold air mass. A few hundred kilometers southeast of this minimum, a surface cyclone is deepening over Malta, staying almost stationary with an occluded front in its northern flank.

At 00:00 UTC, 10 February 2023, this cyclone, showing a low-level WC (not shown), has moved toward the southern tip of Sicily and is associated with an intense surface pressure gradient across Sicily; hence, it produces strong winds, especially in its northern side where easterlies affected the Ionian part of the island. At this time, the upper-level geopotential field shows a wide cyclonic circulation over the central Mediterranean, with the main synoptic cold-core minimum located west of Sardinia, and a small WC cyclone southeast of Sicily. During its deepening, the cyclone took on a symmetric (circular) appearance, forming a warm-air seclusion (Fig. 2). At this stage, very intense rainfall events were recorded in Sicily, with accumulations over 400 mm (maximum of 550 mm in 48 h in Vizzini). Furthermore, given the low temperatures, the precipitation fell in the form of snow at hilly altitudes on the reliefs of eastern Sicily.

At 00:00 UTC, February 11 2023, the cyclone has already weakened, and makes landfall over Africa in a strongly sheared environment, in an area of strong thermal gradient at 500 hPa (intense jet stream), before dissipating rapidly inland.

3.1.2. Satellite analysis

The satellite imagery analysis aims to describe the thermodynamic and microphysical characteristics during the Helios evolution.

Fig. 3 shows the TB imagery of the ATMS high frequency channels for the overpass on 9 February 2023, 11:59 UTC. A south-north oriented convective line extends from the southern Mediterranean to the southeast coast of Sicily. A TB depression is present at 183 ± 7 GHz (Fig. 3b, with values reaching about 200 K), and to a lesser extent at 183± 3 GHz (not shown), highlighting the presence of low density ice particles. No TB depression is evident at 88.2 GHz (Fig. 3a) indicating a weak updraft and lack of heavily rimed, larger ice hydrometeors (graupel) or hail. However, DC is detected in correspondence of the lowest TBs (black dots in Figs. 3a-b) along the south-to-north convective system.

A later AMSR2 overpass occurred on 10 February at 01:02 UTC: if, on one hand, it still evidences the presence of DC, on the other hand indicates a change toward an apparent cyclonic circulation around the minimum mean sea level pressure (MSLP) (Fig. 4). Due to the lack of high-frequency channels, the detection of DC can be inferred from the 89 GHz and 37 GHz Polarization Corrected Temperature (PCT - (Cecil and Chronis, 2018)) depression with respect to the background (Fig. 4a and c). With respect to the ATMS overpass, there seems to be an intensification of the convective activity with an extended PCT depression area and a morphological change in the structure from linear to a curved band convective structure, a first indication of a possible tropical-like transition (although this can be determined only by a joint analysis with the thermal structure). However, it is worth considering the higher spatial resolution of AMSR2 with respect to the ATMS, which allows a more precise depiction of the DC cores. For example, an intense DC core with values as low as 160 K at 89 GHz and 225 K at 37 GHz is clearly visible off the southeastern coastal corner of Sicily (36°N, 15°E). The PCT values at 89 GHz locate the DC cores among the top 1% DC intensity class derived over a 4-year period in the Mediterranean region (Hourngir et al., 2021). The PCT at 37 GHz allows also to detect the precipitation areas, evidenced by a cooling with respect to the background (Fig. 4a), which are confirmed by low values of the difference between the TB at vertical (V) and horizontal (H) polarization channels at 37 GHz (ΔTB_{37GHz}) shown in Fig. 4b. In D'Adderio et al. (2022), $\Delta TB_{37GHz} < 30$ K is set as threshold to identify the precipitation area. According to this, shallow precipitation can be located in the northwestern part of the region close to the minimum MSLP (black cross in Fig. 4), where a ΔTB_{37GHz} lower than 20 K is coupled with high and low PCT values at 89 GHz and 37 GHz, respectively, indicating the presence of intense precipitation with a negligible scattering signal from frozen particles. The confirmation of the lack of ice in the upper levels would be possible with the analysis of higher frequency channels (i.e. ≥166 GHz) that are not available in the AMSR2 radiometer.

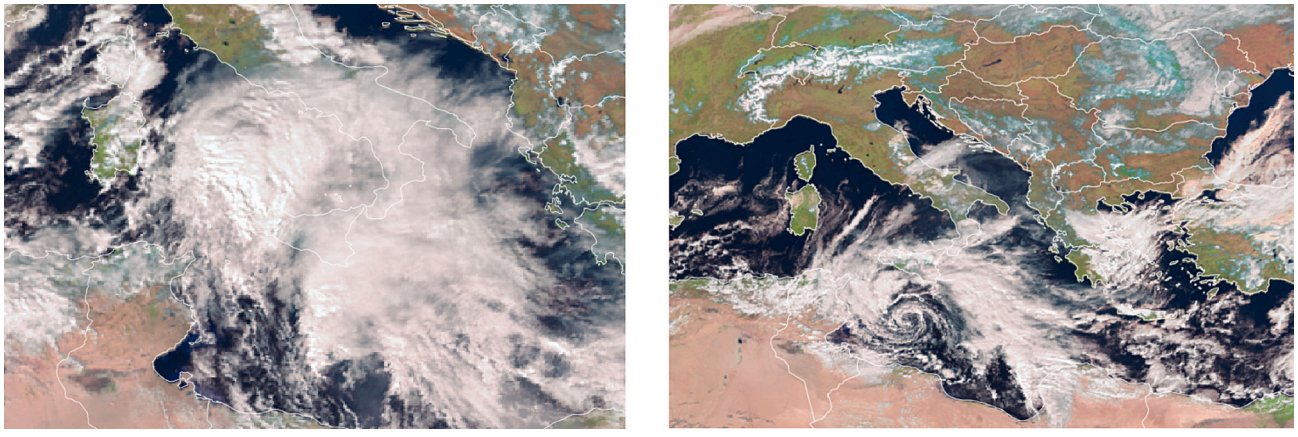

Fig. 1. Satellite SEVIRI RGB composite (using three solar channels: NIR1.6, VIS0.8 and VIS0.6 μm) onboard Meteosat Second Generation (MSG) on 9 February 2023 at 13:00 UTC (left side) and on 10 February 2023 at 12:00 UTC (right side). ©Eumetsat 2023.

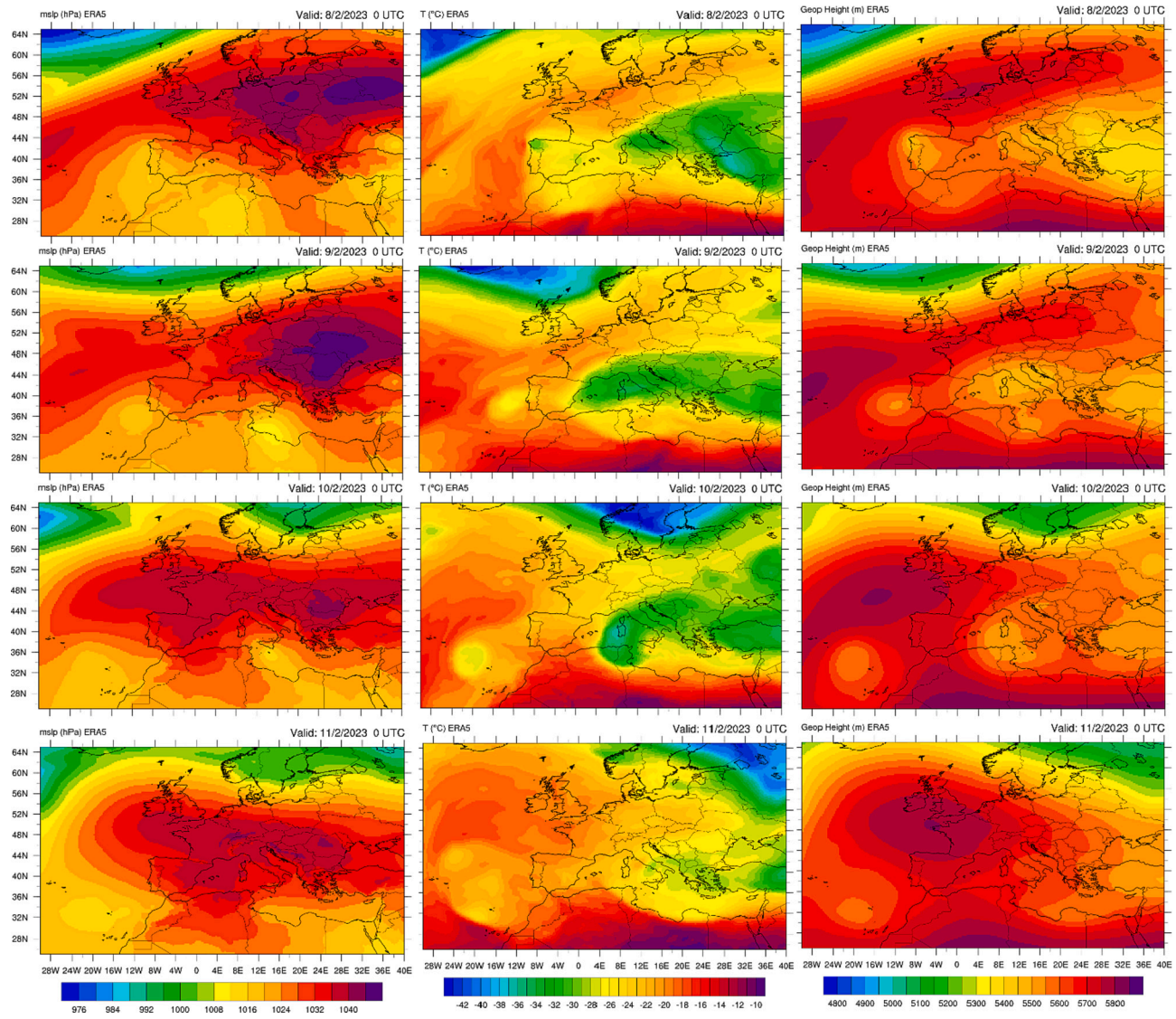

Fig. 2. Mean sea level pressure in hPa (left column), temperature at 500 hPa in Kelvin (middle column) and geopotential height in gpm (right column) charts from 8 February at 00:00 UTC to 11 February at 00:00 UTC.

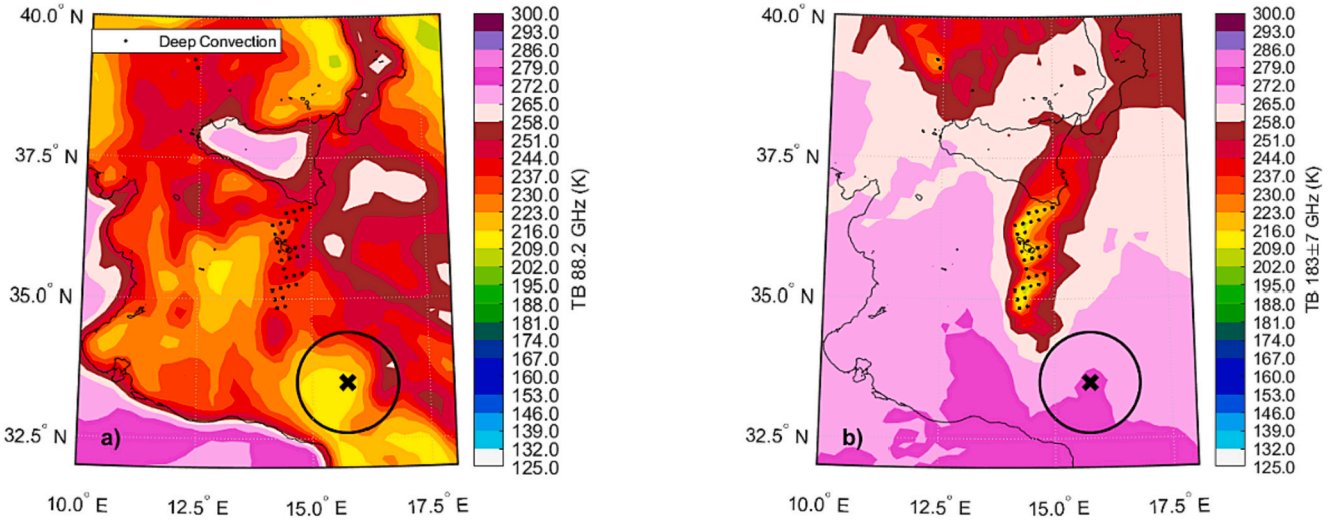

Fig. 3. NOAA 21 ATMS overpass on 9 Feb. 2023 at 11:59 UTC. ATMS TBs at 88.2 GHz (**a**) and 183.31±7 GHz (**b**). Black dots indicate the DC pixels as identified by Hong et al. (2005). The black "x" indicates the location of the minimum MSLP from ERA5, while the black circle indicates the 100 km distance from the minimum MSLP.

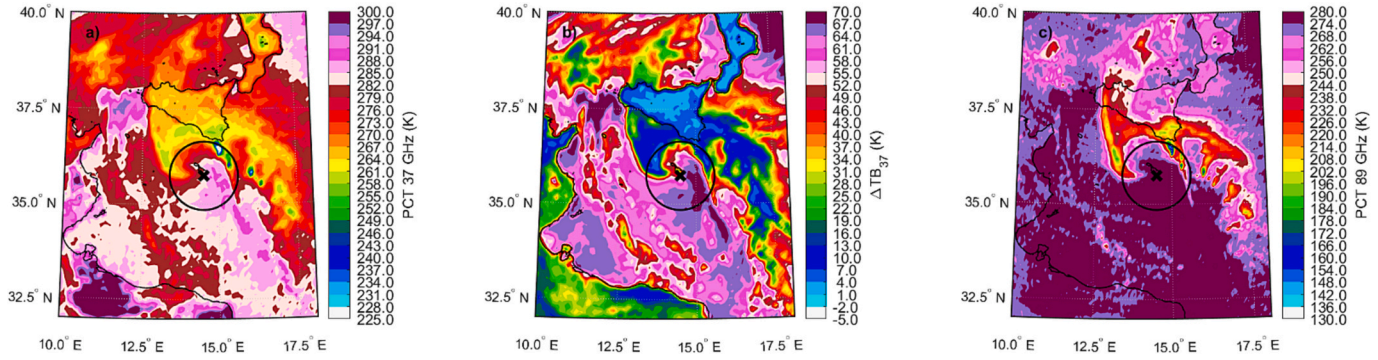

Fig. 4. AMSR2 overpass on 10 Feb. 2023 at 01:02 UTC. Panel (**a**) shows the PCT at 37 GHz, panel (**b**) shows the ΔTB at 37 GHz (i.e. TB_V-TB_H at 37 GHz), and panel (**c**) shows the PCT at 89 GHz. The black "x" indicates the location of the minimum MSLP from ERA5. The black circle indicates the area of 100 km radius around the minimum MSLP.

The analysis of the channel 8/9 for AMSU-A/ATMS (i.e., the 55.5 GHz frequency channel) reveals the presence of stratospheric warm air starting on 9 February (Fig. 5). This channel, having a weighting function peaking at about 200 hPa, is particularly recommended to detect these situations, which are related to dry air intrusions in the upper troposphere (Hoskins et al., 2007). The radiosounding data from Decimomannu station (south coast of Sardinia, 39.35° N, 8.85° E) collected on 9 February 2023 at 12:00 UTC reports the height of the thermal tropopause located between 350 and 200 hPa.

The warm air entered from west/northwest in the region involved in the cyclonic circulation from the morning of 9 February. The warm anomaly overlapped the minimum MSLP region in the early morning of 10 February and in the following hours remained confined above it (Figs. 5f-h).

For the three overpasses showing an isolated warm-air anomaly above the cyclone center (Figs. 5f-h), a warm TB anomaly at mid/upper-troposphere levels (around 600, 400 and 300 hPa) is also present, as highlighted by channels 5–7 and 6–8 for AMSU-A and ATMS, respectively (not shown). The TB anomaly is calculated according to the methodology developed for tropical cyclones (Brueske and Velden,

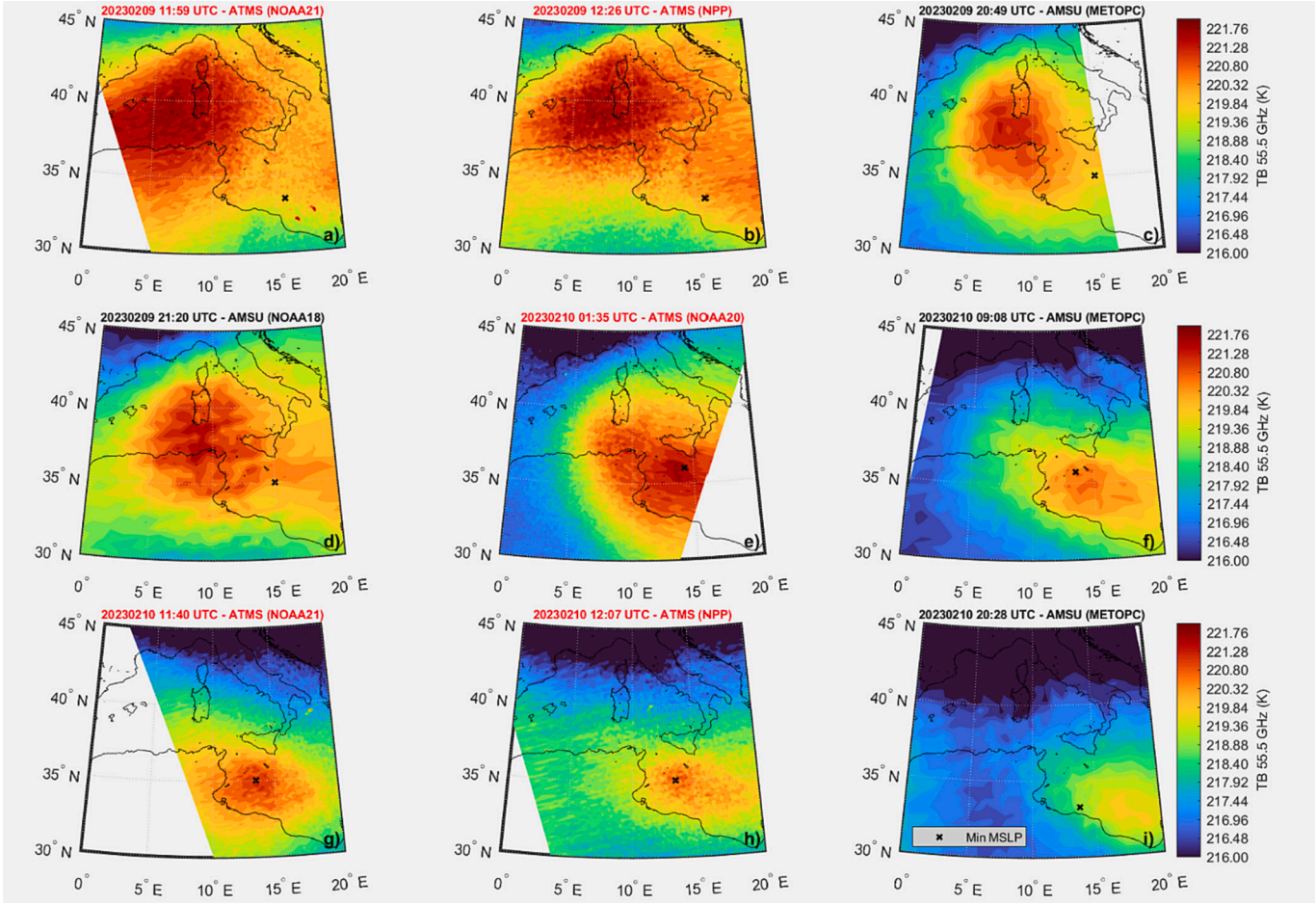

Fig. 5. Sequence of AMSU-A and ATMS overpasses between 9 Feb. 2023 at 00:00 UTC and 10 Feb. 2023 at 23:59 UTC. Panels (**a-i**) show the limb-corrected TB at 55.5 GHz, channel 8 and 9 for AMSU-A and ATMS, respectively. The black "x" indicates the location of the minimum MSLP from ERA5.

2003; Velden and Herndon, 2020) and recently applied to medicanes (Panegrossi et al., 2023). In their work, Panegrossi et al. (2023) defined a WC as very shallow if the warm TB anomaly is visible only in channel 6 (7) (peaking around 400 hPa), shallow if it is visible in channels 6(7) and 7(8) (peaking around 300 hPa), and deep if it is visible in channels 6(7), 7(8), and 8(9) (peaking around 200 hPa) from AMSU(ATMS) measurements. However, as shown in Fig. 5, channel 8(9) of AMSU(ATMS) shows stratospheric warming because of to the low tropopause height approximately located below 200 hPa. For this reason, the TB anomaly analysis is extended to channel 5(6) of AMSU(ATMS) peaking approximately at 600 hPa. Fig. 6 shows the TB anomaly for channels 6–8 of ATMS NPP overpass on 10 February at 12:07 UTC. At first sight, the warm TB anomaly could be associated with a deep WC structure observed in other medicanes, as illustrated in Panegrossi et al. (2023). From a closer inspection, however, some remarkable differences can be noticed. The warm TB anomaly shape is not well defined at least in channels 7 and 8 (i.e., it is not an isolated, circular-like shape typical of medicanes), its spatial extension (i.e., the area with positive TB anomaly) is rather wide and the duration is limited (the temporal lag between the first and the last overpass showing the warm TB anomaly in these channels is about 3 h). A warm TB anomaly is also observed at channel 6 (approximately at 600 hPa). However, this results from the combined effect of the stratospheric air intrusion and of the emission of radiation by the rain droplets, as evidenced by the larger area of warmer TB anomaly compared to the other channels. It can be inferred that the warm TB anomaly observed at all channels (Fig. 6) is associated to warmer air masses in the stratosphere. The decreasing size of the warm anomaly area moving down in the troposphere from channel 9 (Fig. 5h) to channel 8 and 7 (Fig. 6b andc) highlights an intrusion of stratospheric air down to mid-tropopause, and it is in agreement with the synoptic analysis (Fig. 2). Also, we hypothesize that the low sea surface temperature (the event occurred at the beginning of February and the sea surface temperature values were well below 20 °C) may limit the intensity of sea surface fluxes, resulting in weak latent instability and diabatic processes, leading to limited latent heat release in the scattered DC detections as discussed below.

Nearly simultaneously to the ATMS overpass shown in Fig. 6 (i.e., only three minutes before), there was an AMSR2 overpass. The combination of higher spatial resolution at 37 and 89 GHz AMSR2 channels and the 183 ± 7 GHz ATMS channel allows to characterize the cloud and precipitation microphysics during the second phase of Cyclone Helios (Fig. 7). What stands out is the almost total absence of ice (both high- and low-density ice hydrometeors) around the minimum MSLP (which is slightly to the west of the center of the cyclonic circulation depicted by the 37 GHz channel). This is highlighted by the PCT imagery of the AMSR2 at 89 GHz (Fig. 7c) and by the TB imagery of the ATMS at 183 ± 7 GHz (Fig. 7d). Both images show the absence of areas of PCT and TB depression, highlighting the total absence of the contribution from the ice scattering to the upwelling radiation. When the scattering is effective, due to the presence of both heavy and small ice particles, both frequencies show a PCT or TB depression (with respect to the background) as evident in the outer north-eastern rain band hitting south-eastern Sicily (although the lower ATMS spatial resolution does not allow the detection of the small convection cores depicted by AMSR2 - Figs. 7a,c-d). In fact, the areas with PCT values at 89 GHz ≤240 K and TB values at 183 ± 7 GHz ≤260 K, respectively, indicate the presence of ice hydrometeors. These values correspond to the 4th intensity class (accounting for 10% lowest PCT values) of the DC feature classification provided by Hourngir et al. (2021). This confirms a weakening of the convective activity with respect to the previous phase when the PCT values fall in the 3rd intensity class (accounting for 1% lowest PCT values). On the other hand, higher values highlight the negligible presence or total absence of ice hydrometeors. Consequently, the precipitation areas identified by both PCT and ΔTB_{37GHz} (Figs. 7a-c) over sea (by values respectively lower than about 270 K and 30 K, respectively) can be labeled as mostly warm rain processes. This feature was already detected during the tropical-like phase of other medicanes (D'Adderio et al., 2022; Dafis et al., 2020; Marra et al., 2019; Miglietta et al., 2013; Panegrossi et al., 2023), but it was limited to the inner region around the cyclone center. Here the total absence of convection and mixed phase precipitation is evident in a wide area corresponding to the warm TB anomaly shown in Fig. 6. It has to be also highlighted that the low tropopause height is an additional factor limiting the vertical extension of DC cores. A further confirmation of what is revealed by the PMW imagery is provided by the CTH and IWP estimated by the DEEPSTORM algorithm (Fig. 7e-f). The CTH shows a very limited vertical extent of the clouds near the cyclone center, with values not exceeding 7 km, and slightly higher values on the eastern rain band (Fig. 7e). At the same time, the lack of a cloud-free eye is also evident from the CTH analysis, which is in contrast with the cloud structure of other medicanes' mature phases (see Panegrossi et al. (2023) - Fig. 2c). Also a visual inspection from the VIS channel of MSG SEVIRI highlights the cyclonic circulation together with the absence of a well defined cloud-free eye (Fig. 1). On the other hand, the IWP estimation confirms the lack of ice around the cyclone center and in the northwestern precipitation area, while higher values (up to 4.5 kg m^{-2}) are found in the eastern rain band. Fig. 7 also shows the presence of an intense precipitation band in the northeastern cyclone quadrant affecting the southeast corner of Sicily. The associated AMSR2 surface precipitation rate estimate (Casella et al., 2017) (i.e., delivered operationally as auxiliary product within the EUMETSAT H SAF, hereafter labeled as H-AUX-17), confirms very light precipitation rates (generally lower than 3 mm h^{-1}) close to the cyclone center and higher values in the outer rain band (Fig. 8). H-AUX-17 is a very suitable PMW H SAF precipitation product

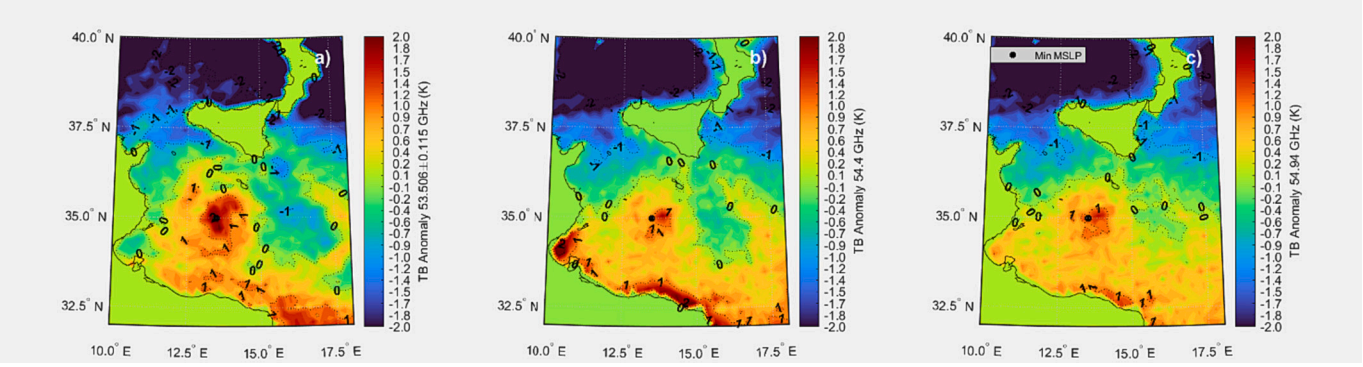

Fig. 6. ATMS NPP limb-corrected TB anomaly over sea (land pixels are flagged at 0 K) for channels 6 (**a**), 7 (**b**), 8 (**c**) with scattering correction, for the overpass on 10 Feb. 2023 at 12:07 UTC. The black "x" indicates the location of the minimum MSLP from ERA5.

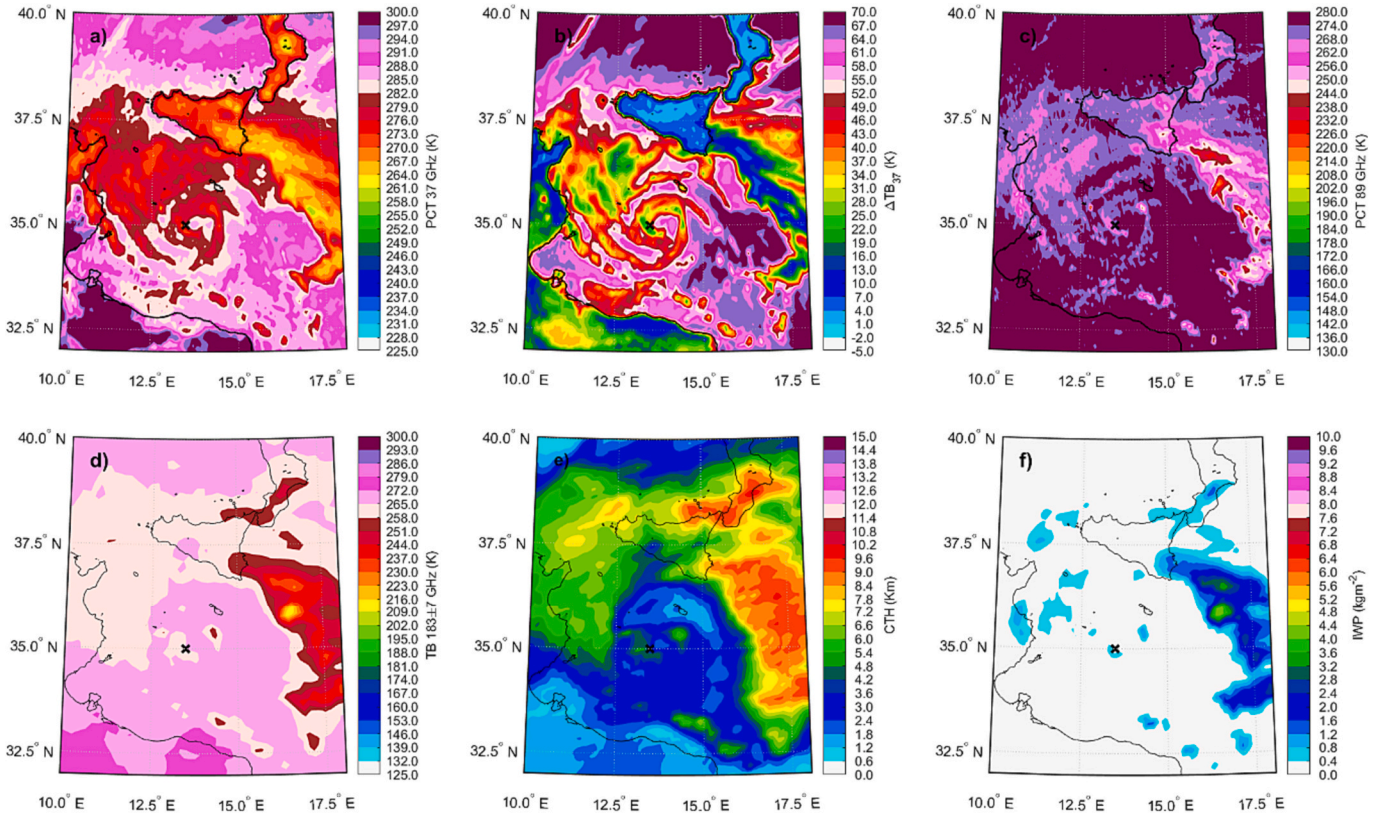

Fig. 7. Panel (**a**) reports the PCT at 37 GHz, (**b**) the ΔTB at 37 GHz and (**c**) the PCT at 89 GHz for the AMSR2 overpass on 10 Feb. 2023 at 12:04 UTC. Panel (**d**) reports the TB at 183 ± 7 GHz for the NPP ATMS overpass on 10 Feb. 2023 at 12:07 UTC. Panel (**e**) and (**f**) report the CTH and the IWP as estimated by the DEEPSTORM algorithm. The black "x" indicates the location of the minimum MSLP from ERA5.

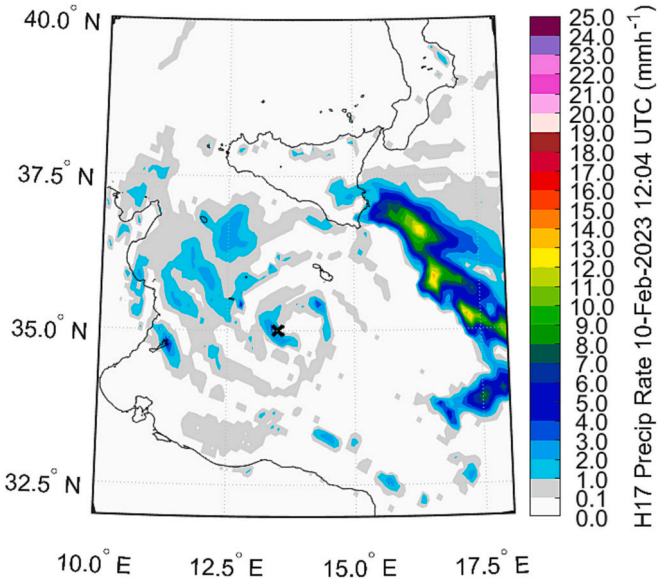

Fig. 8. Instantaneous precipitation rate estimated by the P-IN-AMSR2 H SAF auxiliary product for the AMSR2 overpass on 10 Feb. 2023 at 12:04 UTC. The black "x" indicates the location of the minimum MSLP from ERA5.

to detect and estimate shallow/warm rain over the sea because of the exploitation of low-frequency channel measurements, sensitive to the rain droplet emissions over the radiatively cold sea surface, and because of the high spatial resolution of AMSR2 (comparable to the GMI) able to resolve even the smaller scale precipitation features.

3.2. Cyclone Juliette: 27 February-3 March 2023

Juliette was a long-lasting cyclone, which originated on 26 February 2023 from the collision of cold air coming from northeast Europe and warmer and humid air coming from southwest Europe. Juliette lasted for several days, as it disappeared from numerical model outputs only after 3 March 2023. Here, we focused on the period between 27 and 28 February 2023, when, similarly to Helios, it was affected by a stratospheric air intrusion. However, it shows a cyclonic circulation on 28 February and 1 March 2023 as highlighted by the VIS channel of MSG SEVIRI (Fig. 9).

3.2.1. Synoptic analysis

At 00:00 UTC, 26 February 2023, the 500 hPa geopotential height map (Fig. 10) shows a cut-off low positioned over the western Mediterranean, separated from a polar air mass over northeast Europe within a deep long-wave trough moving fast to the southwest. At low levels, a cyclonic circulation affects the central Mediterranean basin, at the southern edge of the long-wave trough that reaches the Mediterranean. The Mediterranean cyclone develops in a strong baroclinic zone, at the boundary between a cold/dry air mass driven by the northerly flow on the east side of an anticyclone centered on the British Isles, and warm/humid air advected from northern Africa.

Over the next 24 h, the surface low intensifies, while its center moves west of Sardinia. At 500 hPa, the elongation of the trough toward Iberia and the associated cold advection on the southern side of the anticyclone reinvigorate the minimum, now centered between Spain and France.

At 00:00 UTC, 28 February 2023, the surface cyclone intensifies further and is positioned between the Balearic Islands and Sardinia, thus remaining nearly stationary, with a slight westward drift. In this phase, it starts to be vertically aligned with the upper level cold-core low; the associated cold air has penetrated the western Mediterranean, favoring

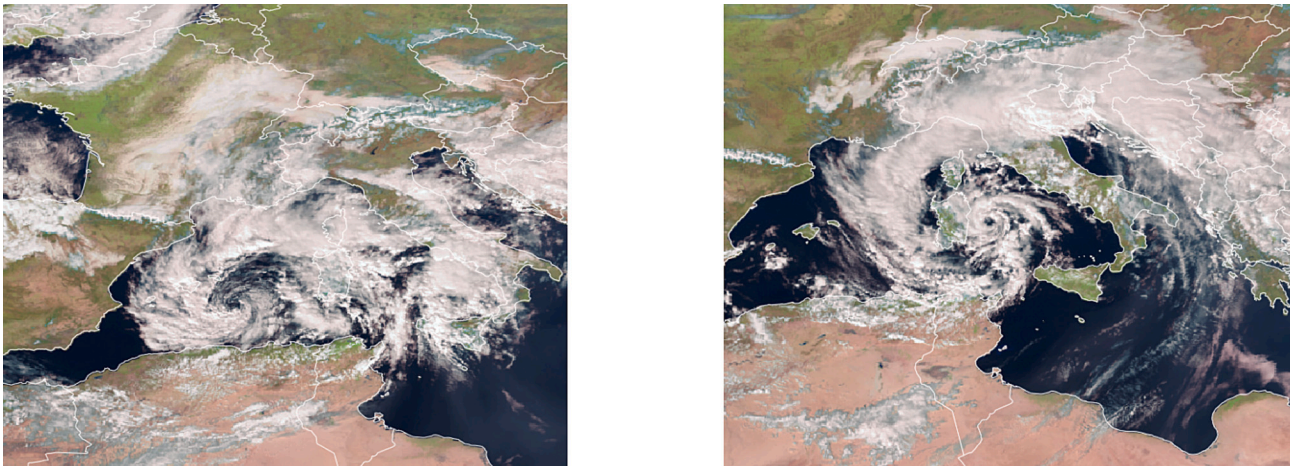

Fig. 9. Satellite SEVIRI RGB composite (using three solar channels: NIR1.6, VIS0.8 and VIS0.6 μm) onboard Meteosat Second Generation (MSG) on 28 February 2023 at 13:00 UTC (left side) and on 1 March 2023 at 13:00 UTC (right side). © Eumetsat 2023.

gale-force wind, rainfall, and even snowfall at very low altitudes in the Balearic Islands.

Following the jet stream, the cyclone starts to move east-southeastward, so that at 00:00 UTC, 1 March 2023, it is centered near the southwest tip of Sardinia; then, it weakens after crossing Sardinia, and at 00:00 UTC, 2 March 2023 it is positioned over the Tyrrhenian Sea, near the east coast of Sardinia, before making landfall between Corsica and Sardinia, where it finally disappears on 3 March.

3.2.2. *Satellite analysis*

Considering the whole lifetime of Juliette, from 26 February to 3 March 2023, a remarkably high number (>50) of satellite overpasses (namely, AMSU and ATMS) are available.

The analysis of TB at channel 8/9 of AMSU-A/ATMS for some of the overpasses available over the study area between 27 February and 1 March, shows the intrusion of stratospheric warm air into the Mediterranean region approaching from the west (i.e., South France and Pyrenees – Fig. 11). The radiosounding data collected from the Cuneo station (44.53° N, 6.71° E) show a tropopause between 270 and 250 hPa. In this case, a warm anomaly occurred since the first hours of 27 February (Figs. 11a-b), overlapping the minimum MSLP region only since 28 February (Figs. 11f-g). The strength and the spatial extension of the warm-air anomaly are comparable to that for Helios, that is a maximum TB around 222–224 K and a horizontal extent of roughly 5°x5°, respectively. However, starting on 28 February at 20:57 UTC, the TB anomaly weakens and almost completely dissipates on 1 March (Figs. 11i-l). This would be the period where tropical transition could be more likely, but to be able to assess if it actually occurred both the cloud features and the thermal structure between the 28 February and the 1 March are analyzed below.

In order to characterize the cloud and precipitation microphysics (within the cyclone center and on the outer rain bands) and to relate it to the WC development, the high frequency MHS/ATMS channel TBs (i.e. 183 ± 7 GHz) for all the available overpasses between 28 February and 1 March, are reported in Fig. 12. The overpasses shown here are more frequent than in Fig. 11: since the study area is covered by the edge of the swath and the 50 GHz channels have lower resolution than high frequency channels (i.e. >89 GHz), the detection of the WC is more problematic. Fig. 12 shows the scarce occurrence and scattered areas of TB depression, due to the presence of ice hydrometeors in the region surrounding the cyclone center (i.e. within 100 km). While, the first two overpasses (Figs. 12a-b) do not show any scattering signal, a slight TB cooling is visible in the remaining overpasses (within 100 km radius from the center) until 28 February at 13:11 UTC (Fig. 12f), suggesting the presence of small amounts of ice and limited convective activity. This is also confirmed by the lack of DC pixels (according to the Hong et al. (2005) methodology) for these overpasses.

A GMI overpass on 28 February 2023, 16:42 UTC further supports the lack of convective activity in this stage, and the presence of scattered areas with low density ice hydrometeors as evidenced by the TB cooling at 166 GHz and a negligible TB cooling at 89 GHz (Fig. 13). Following the methodology in D'Adderio et al. (2022), the DC detection occurred only in the outer rain bands (and in a very limited area) during this stage of the cyclone lifetime (red dots in Fig. 13d). Moreover, Fig. 13d shows that, within the cyclone center, ice is found in a limited number of pixels (labeled as "ice on top", green dots). At the same time, due to the lack of warm rain (magenta dots are not present), the precipitation (blue dots) is likely mostly stratiform (i.e. pixels where both rain and ice on top are detected).

The later overpasses, starting on 28 February at 20:56 UTC (Fig. 12g), show larger areas with ice (scattering signal at 183 ± 7 GHz) in proximity of the cyclone center, and on 1 March at 01:29 UTC (Fig. 12h) DC pixels are detected in the proximity of the cyclone center. The following and final stages of Juliette, roughly 1–3 March 2023, show a persistent cyclonic circulation with a progressive deepening of DC activity in proximity of the cyclone center (i.e. TB cooling at both 166/183 GHz and 89 GHz channels, not shown).

It is worth noting that once the upper-level warm anomaly overlaps the minimum MSLP region (Figs. 11f-l), a WC structure develops at lower levels. On 28 February at 01:48 UTC the WC between about 600 and 300 hPa (i.e. at channels 5–7 and 6–8 for AMSU-A and ATMS, respectively) is not well defined, with an irregular shape and a bulging in the southeast direction (Figs. 14a-c). The overpass that occurred at 12:19 UTC on 28 February 2023 (Figs. 14d-f) evidences a quite well-identified WC at channel 7–8 (Fig. 14e-f). It is worth noting that the stronger WC signal (higher TB anomaly values) evidenced by ATMS channel 6 (53.596 GHz) for all the overpasses is also due to the impact of the radiation emission by the rain droplets, which contributes to increase the TBs. As a matter of fact, the pattern of the TB anomaly follows the cyclone rain bands. On 1 March at 01:30 UTC (Figs. 14g-i), when Juliette passed through the Sardinia channel to reach the central Tyrrhenian Sea, the WC is reduced in size although the signal is contaminated by the radiatively warm land surface. The WC persists and becomes deep on 1 March, at 12:25 UTC and it is clearly visible at all channels (Figs. 14j-l and Fig. 11l).

Summing up, the weakening of the warm TB anomaly at higher levels during the whole lifetime of Juliette (Fig. 11) along with the onset of the warm TB anomaly at lower levels starting on 28 February (Fig. 14) is an indication of a possible tropical transition with a WC development. The WC originates as shallow on 28 February and becomes deep on 1 March.

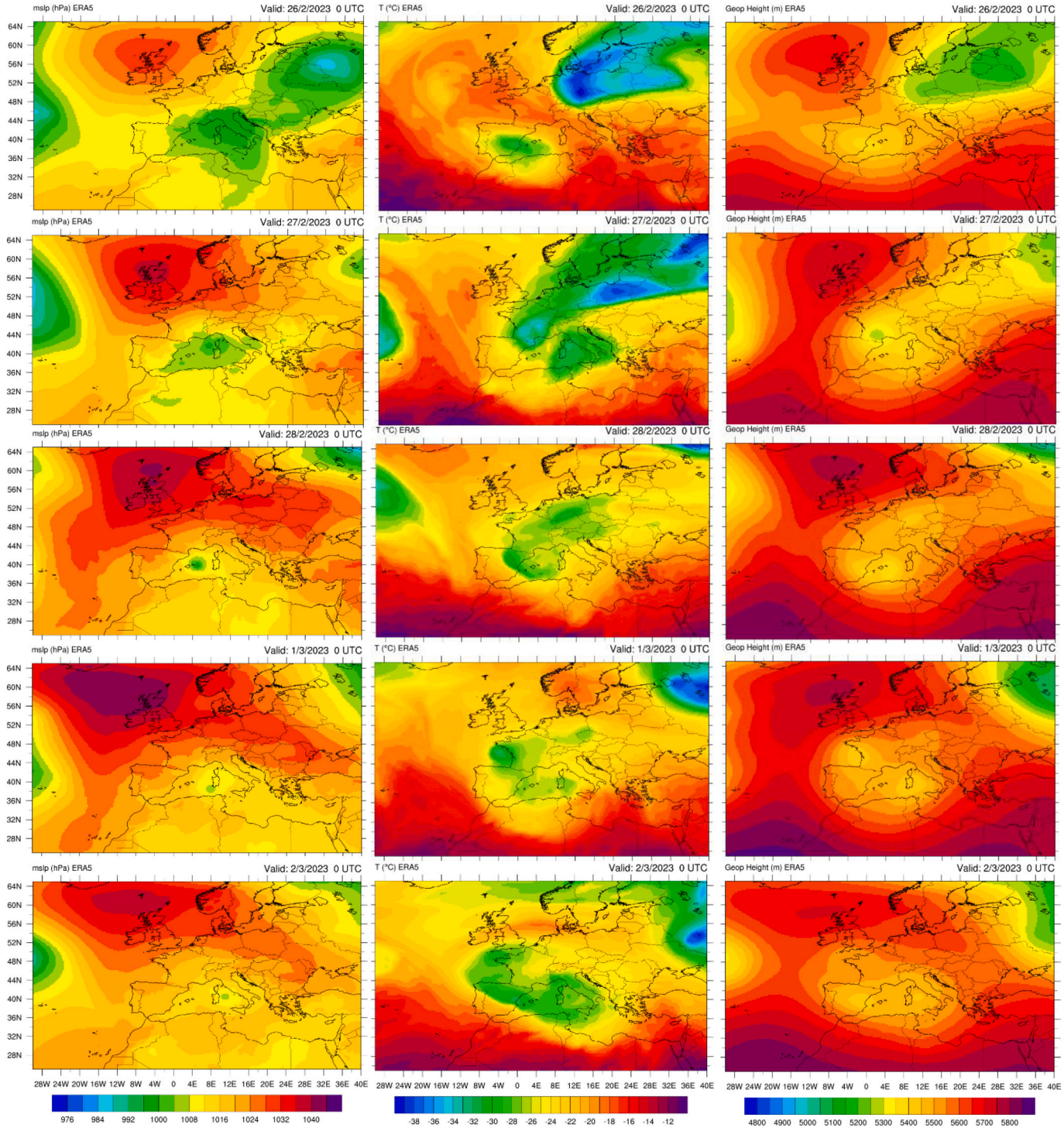

Fig. 10. Mean sea level pressure in hPa (left column), temperature at 500 hPa in Kelvin (middle column) and geopotential height in gpm (right column) charts from 26 February at 00:00 UTC to 2 March at 00:00 UTC.

The WC undergoes weakening and strengthening phases between the afternoon of 1 March to the night of 2 March depending on the occurrence of DC in proximity of cyclone center. The cyclone did not have the space to intensify further, given the proximity to the land surface and the cold sea surface temperature (~14 °C). The presence of DC in the proximity of the cyclone center on 1 March at 01:30 UTC (Fig. 12h) as well as on 2 March (not shown) is a good indication that the WC was mainly driven by diabatic processes and that a tropical-like transition took place at this stage.

While the satellite image sequence in Fig. 14 evidences the deepening of the cyclone and a possible tropical transition on 1 March, the DEEPSTORM-based CTH for the same overpasses highlights the presence of a nearly closed cloud-free eye (Fig. 15). The size of the eye progressively reduces (Fig. 15 a–d) as the WC develops and intensifies (Figs. 14 going from the top to the bottom in each column). The CTH shows a nearly closed cloud-free eye on March 1 at 12:25 UTC (with respect to the previous phase the eye results to be more defined, smaller and almost completely closed, also looking at the VIS channel of MSG

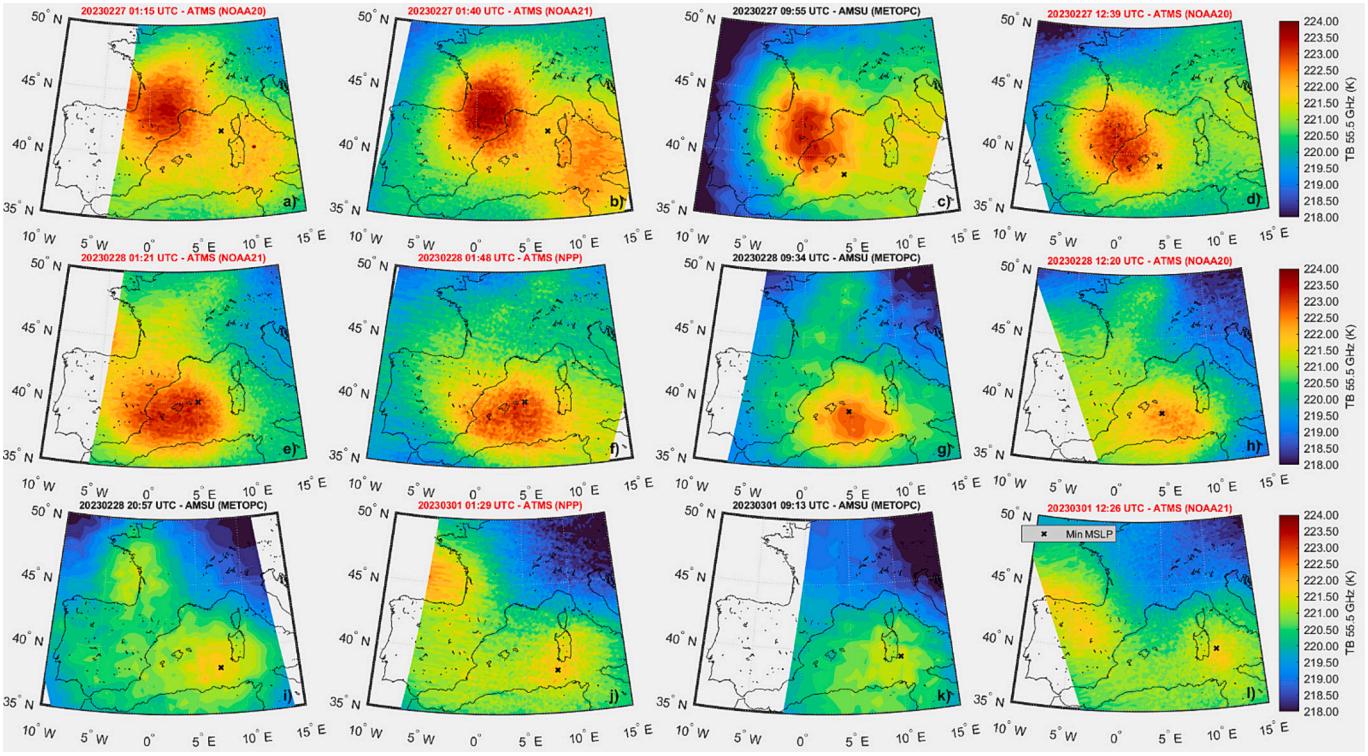

Fig. 11. Sequence of AMSU-A and ATMS overpasses between 27 Feb. 2023 at 00:00 UTC and 1 Mar. 2023 at 12:26 UTC. Panels (**a-l**) show the limb-corrected TB at 55.5 GHz, channel 8 and 9 for AMSU-A and ATMS, respectively. The black "x" indicates the location of the minimum MSLP from ERA5.

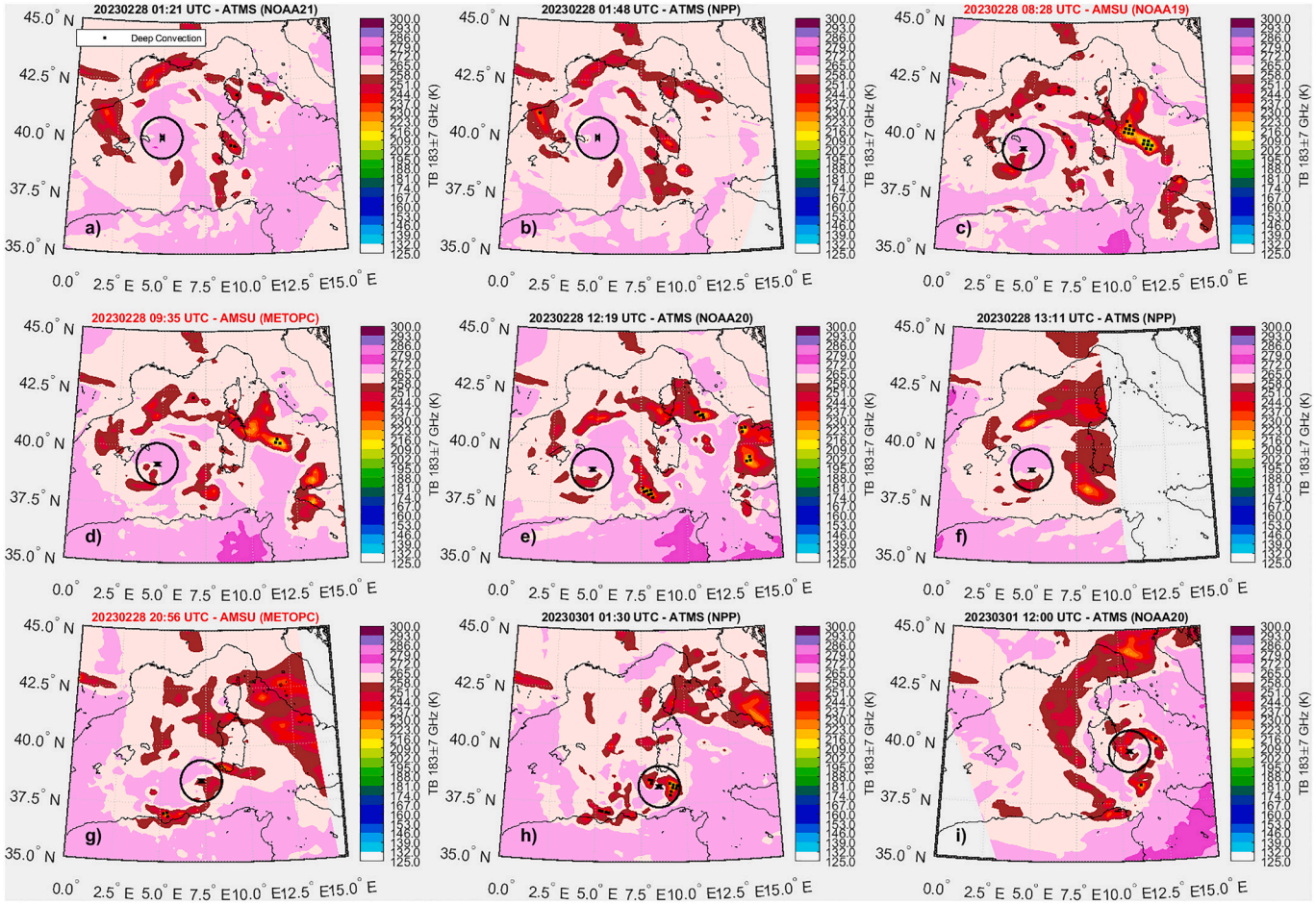

Fig. 12. Sequence of AMSU-A and ATMS overpasses between 28 Feb. 2023 at 00:00 UTC and 1 Mar. 2023 at 12:00 UTC. Panels (**a-i**) show the TB at 183 ± 7 GHz channel. The black "x" indicates the location of the minimum MSLP from ERA5,the black dots indicate the pixels characterized by DC. The black circle indicates the area of 100 km radius around the minimum MSLP.

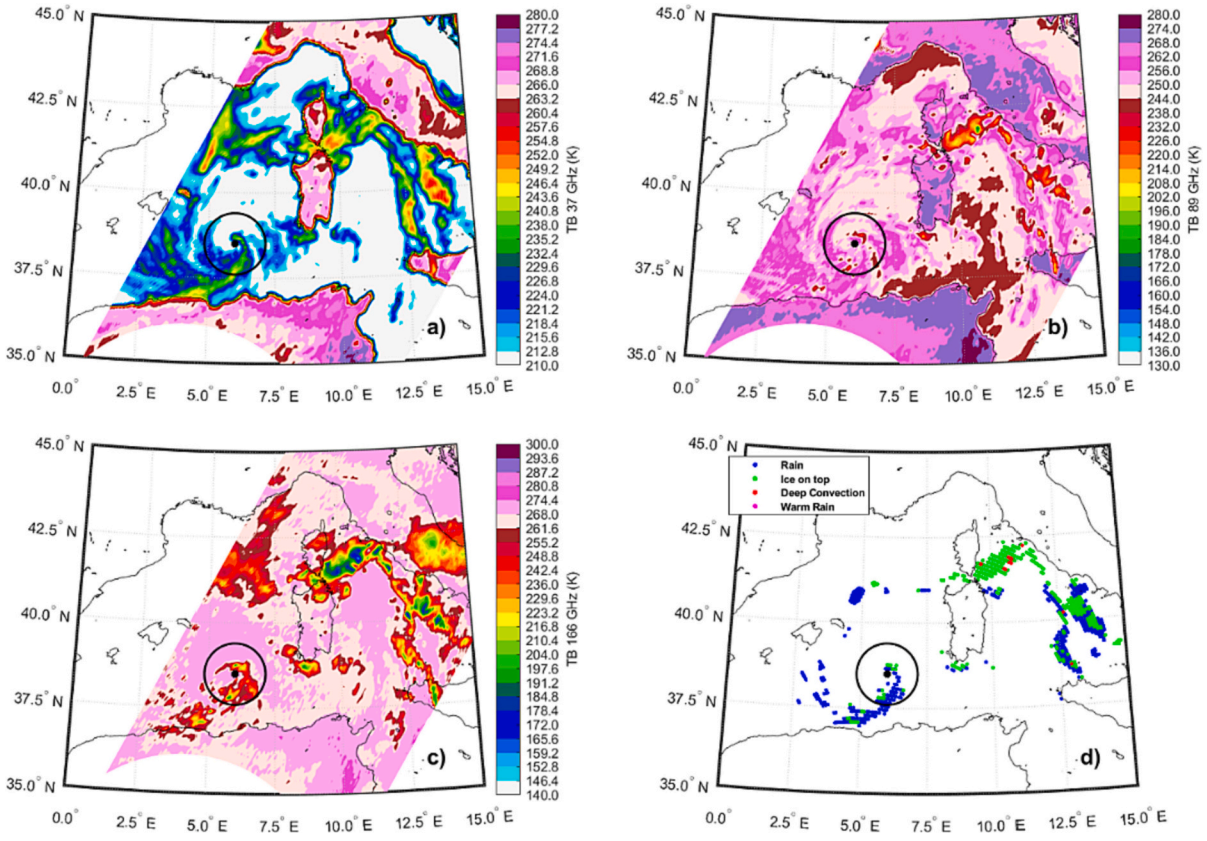

Fig. 13. GMI TB imagery at 37 GHz (**a**), 89 GHz (**b**), and 166 GHz (**c**), and cloud and precipitation classification according to the methodology developed in (D'Adderio et al., 2022) for the GMI overpass on 28 Feb. 2023 at 16:42 UTC. The black "x" indicates the location of the minimum MSLP from ERA5, while the black circle indicates 100 km distance from the minimum MSLP.

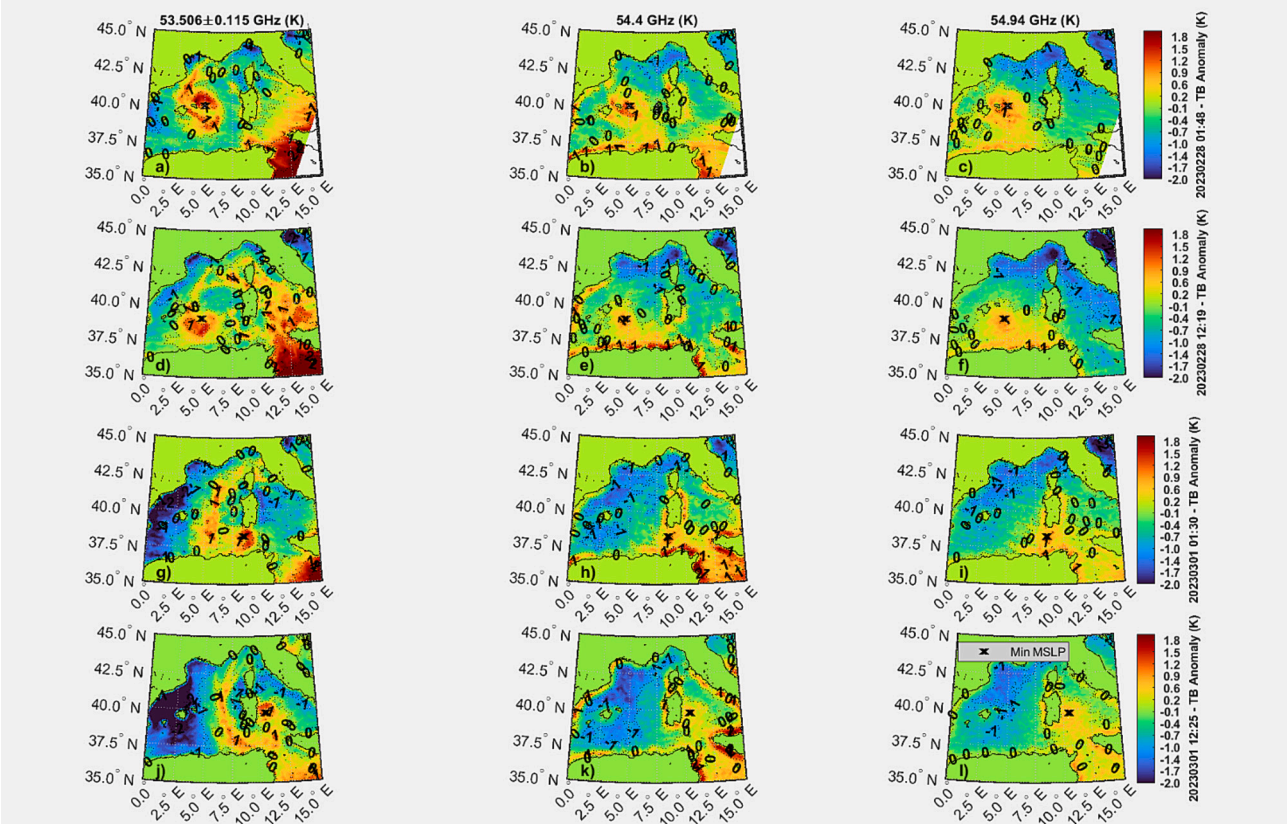

Fig. 14. ATMS limb-corrected TB anomaly over sea (the land surface is flagged to 0 K) for channels 6 (left column), 7 (middle column), 8 (right column) with scattering correction, for the overpasses on 28 Feb. 2023 at 01:48 UTC (panels a-c), on 28 Feb. 2023 at 12:19 UTC (panels d-f), on 1 Mar. 2023 at 01:30 UTC (panels g-i) and on 1 Mar. 2023 at 12:25 UTC (panels j-l). The black "x" indicates the location of the minimum MSLP from ERA5.

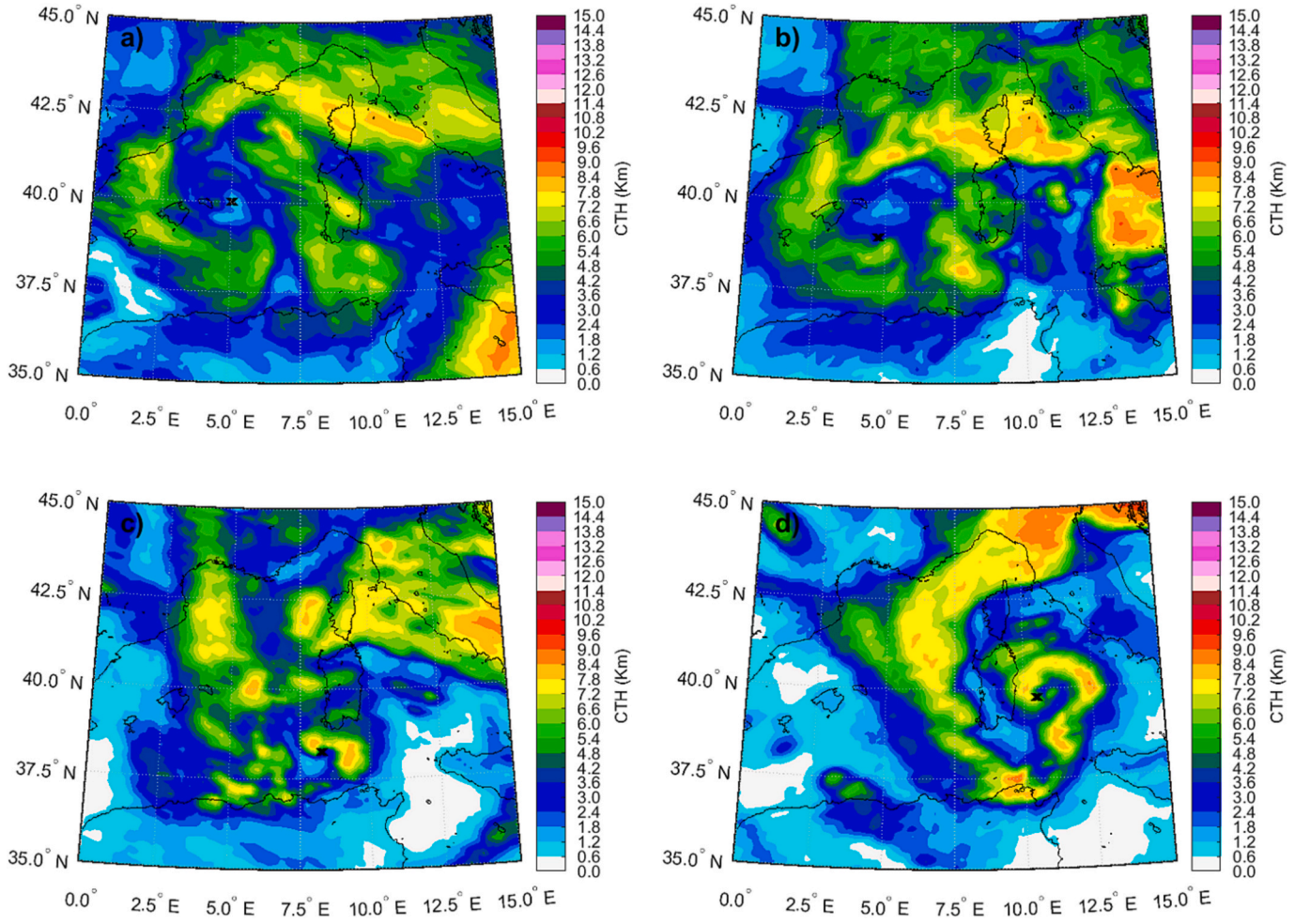

Fig. 15. CTH estimated by DEEPSTORM algorithm for (a) ATMS NPP overpass on 28 Feb. 2023 at 01:48 UTC, (b) ATMS NOAA-20 overpass on 28 Feb. 2023 at 12:19 UTC, (c) ATMS NPP overpass on 1 Mar. 2023 at 01:29 UTC and (d) ATMS NOAA 21 overpass on 1 Mar. 2023 at 12:25 UTC. The black "x" indicates the location of the minimum MSLP from ERA5.

SEVIRI, except in the northeastern side - Fig. 15d and Fig. 9, respectively), which is missing between March 2 and March 3 (not shown). At this stage, the cyclone thermal structure shows the disappearance of the upper-level warm anomaly, and the progressive weakening of the WC signal.

4. Discussion and conclusions

In this paper, we investigated two Mediterranean cyclones, named Helios and Juliette, that occurred between the beginning of February and the beginning of March 2023. Both events have been analyzed both from a synoptic point of view and from an observational perspective, trying to build a link between the dynamics and the thermodynamics and the microphysical properties derived from satellite PMW-based diagnostics.

Helios and Juliette are characterized by a very similar evolution, having both originated by the collision of low/mid-tropospheric cold air mass, coming from northeast Europe, with warmer air masses present over the Mediterranean area. The synoptic analysis shows that both cyclones are characterized by surface depression with different frontal systems well-evident during their maximum intensity phase. At higher levels, stratospheric warming occurred in both cases. This is clearly evidenced by the temporal evolution of TB measured at 55.5 GHz (peaking around 200 hPa) channel from both AMSU and ATMS overpasses. Both cyclones show the development of a warm-air anomaly in the lower stratosphere and in the mid-upper troposphere (i.e. at about 400 and 300/250 hPa, respectively, corresponding to 54.4 and 54.94 GHz channels), when the stratospheric warm air overlaps the surface low. Thus, the presence of a warm and dry anomaly (the analysis of the water vapor absorption channel, 183.3 ± 1 GHz, highlights this aspect - not shown) in the upper-troposphere foresees the development of a not well-defined WC at lower (mid-tropospheric) levels. The presence of a vertical cyclone tilt at early stages is characteristic of the extratropical phase, and suggests that the baroclinic instability is very important at the initial stages. The vertical alignment in the following phase suggests the evolution either into a warm seclusion, or into a tropical-like cyclone (more barotropic environment). The application of Hart diagram (Hart, 2003) to ERA5 reanalysis data confirms the presence of a deep WC for a limited period in both cyclones. The results of the present paper highlight the importance of PMW sensors in discriminating between the categories of diabatically-driven WC (i.e., tropical-like cyclones) and warm seclusions, which cannot be separated by using exclusively the Hart diagram, as discussed in (Miglietta and Rotunno, 2019).

The evolution of Helios and Juliette is in agreement with that of five out of the six medicanes analyzed in Panegrossi et al. (2023). As an example, Figs. 16 and 17 show the stratospheric warming from southwest and northwest of the surface low for Qendresa and Zorbas, respectively, as highlighted by the 55.5 GHz AMSU and ATMS channel evolution. As evidenced for Helios and Juliette, also for Qendresa and Zorbas the WC developed at lower levels (a shallow WC for the former, and deep WC for the latter has been reported in Panegrossi et al. (2023)) once the surface low is in phase with the upper-level warm-air anomaly.

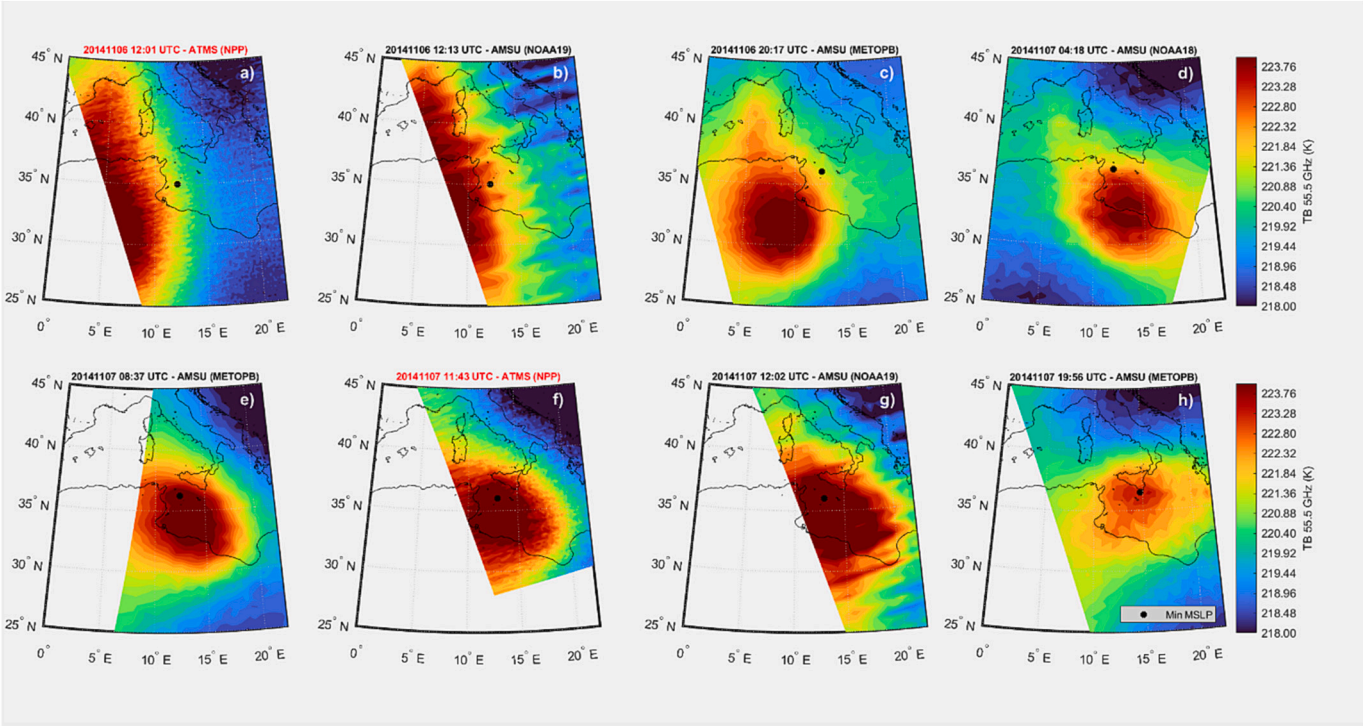

Fig. 16. Sequence of AMSU-A and ATMS overpasses between 6 Nov. 2014 at 12:01 UTC and 7 Nov. 2014 at 19:56 UTC (Medicane Qendresa). Panels (**a-h**) show the limb-corrected TB at 55.5 GHz, channel 8 and 9 for AMSU-A and ATMS, respectively. The black "x" indicates the location of the minimum MSLP from ERA5.

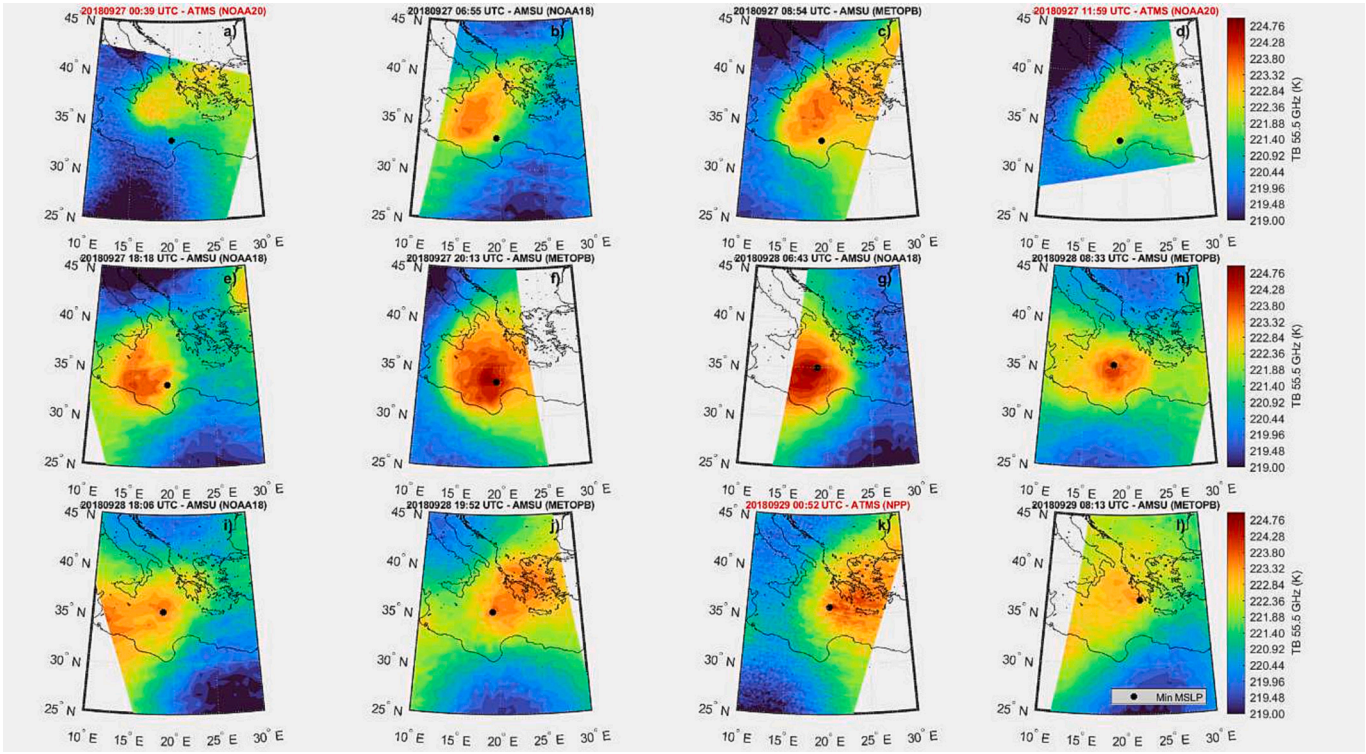

Fig. 17. Sequence of AMSU-A and ATMS overpasses between 27 Oct. 2018 at 00:39 UTC and 29 Oct. 2018 at 08:13 UTC (Medicane Zorbas). Panels (**a-l**) show the limb-corrected TB at 55.5 GHz, channel 8 and 9 for AMSU-A and ATMS, respectively. The black "x" indicates the location of the minimum MSLP from ERA5.

Conversely, the only case that shows a different behavior is Medicane Ianos. As highlighted in Fig. 18, the development stages (Fig. 18a-c relative to 16 September 2020) of Ianos are characterized by the lack of a large-scale stratospheric warm anomaly (absence of TB warming in the 55.5 GHz channel), which becomes evident for the ATMS overpass occurred on 17 September 2020 (see Panegrossi et al. (2023) for more details). However, a combined analysis of Figs. 18 and 19 (reporting the time evolution of 54.4 GHz channel) shows clearly the development of a

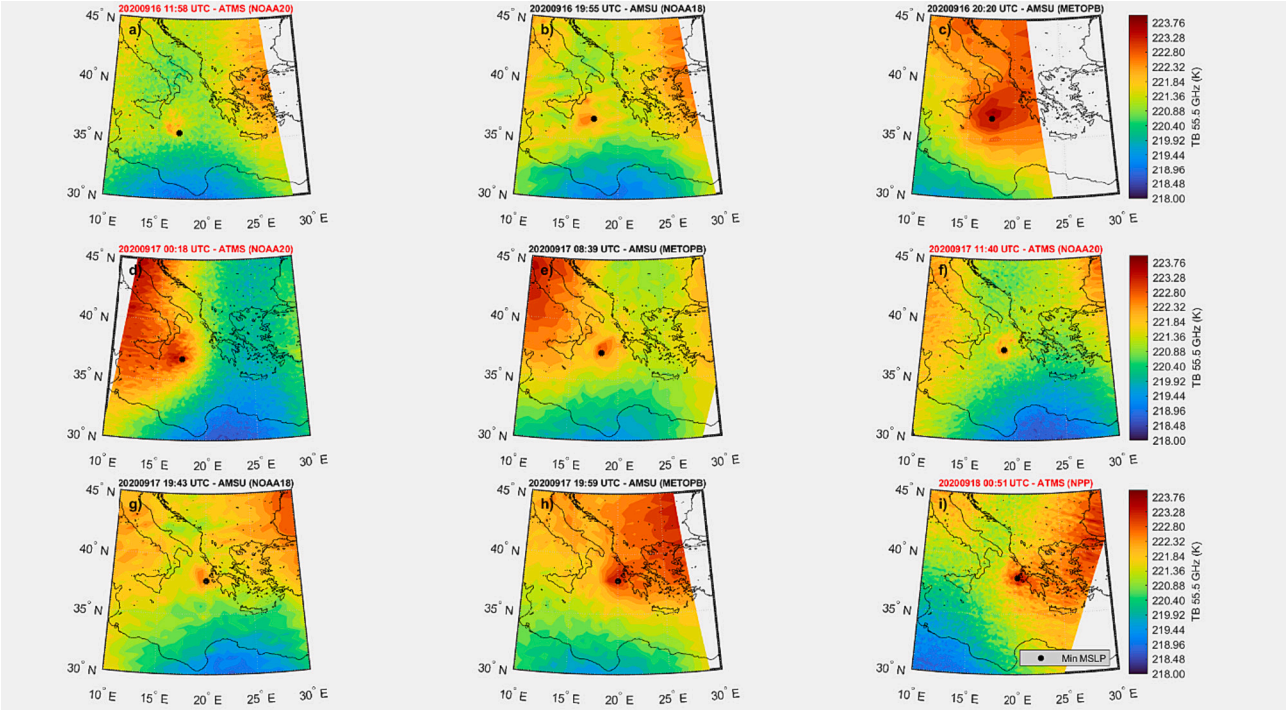

Fig. 18. Sequence of AMSU-A and ATMS overpasses between 16 Sep. 2020 at 11:58 UTC and 18 Sep. 2020 at 00:51 UTC (Medicane Ianos). Panels (**a-i**) show the limb-corrected TB at 55.5 GHz, channel 8 and 9 for AMSU-A and ATMS, respectively. The black "x" indicates the location of the minimum MSLP from ERA5.

deep WC already in the first phase of Ianos. The NOAA18 AMSU-A overpass that occurred on 16 September 2020 at 19:55 UTC shows a well-defined WC at lower levels (Fig. 19b), but not at higher levels (Fig. 18b). Later on, namely the overpass that occurred on 17 September 2020 at 08:39 UTC is the first one where the WC is well defined, stronger (higher TB values) and even with a slightly larger structure at both 55.5 and 54.4 GHz (Figs. 18d and 19d).

On the other hand, the analysis of the time evolution of the 54.4 GHz channel signal (Fig. 19) highlights the transition of Ianos from a DC system (low TB cores close to the minimum MSLP are clearly visible

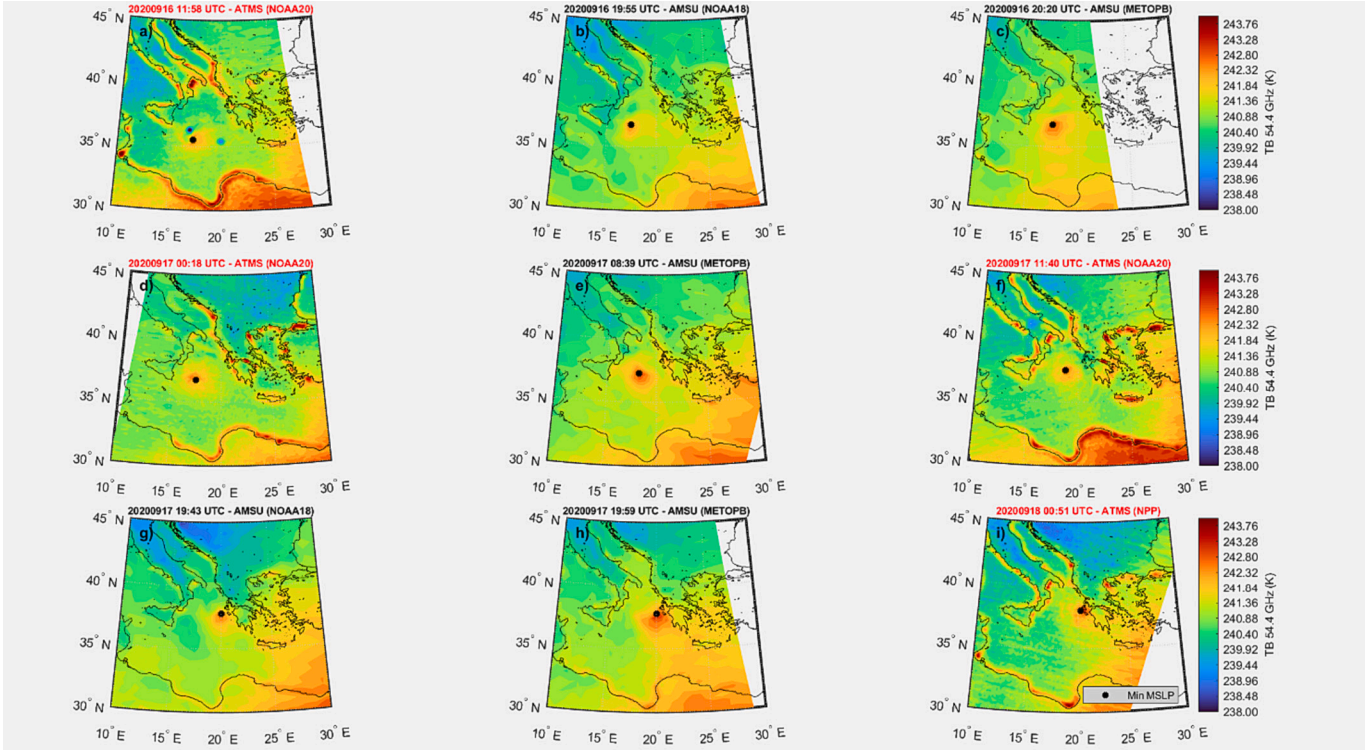

Fig. 19. Sequence of AMSU-A and ATMS overpasses between 16 Sep. 2020 at 11:58 UTC and 18 Sep. 2020 at 00:51 UTC (Medicane Ianos). Panels (**a-i**) show the limb-corrected TB at 54.4 GHz, channel 6 and 7 for AMSU-A and ATMS, respectively. The black "x" indicates the location of the minimum MSLP from ERA5.

Fig. 19a) to a medicane with a bottom-top WC development (i.e., the development of the warm anomaly occurs in the lower levels before the large-scale upper-level warm anomaly affects the region above the cyclone). The WC can be identified in the lower levels already in the first stages of the cyclone lifetime (Fig. 19a-b). At this time, the WC structure is, indeed, isolated and quite well-defined (i.e. circular shape), features that will be strengthened in the next phases of Ianos evolution.

If, on one hand, Helios and Juliette show a thermodynamic behavior comparable to that of most medicanes, on the other hand they do not present the same microphysical properties. Both cyclones show the predominance of shallow precipitation. Helios shows the total absence of DC features in the region of the warm anomaly of stratospheric origin around their center. The analysis of high frequency channels from MHS and ATMS, as well as the analysis of AMSR2 and GMI providing measurements of the precipitation structure and microphysics at higher spatial resolution, reveals the absence of any features related to DC development. The absence of DC seems to confirm that the diabatic processes did not play a key role and the vertical alignment of the warm TB anomaly and suggests its evolution into a warm seclusion. On the other hand, for Juliette PMW measurements evidence the onset of DC in the proximity of the cyclone center, although not very intense, coupled with the presence of low-density ice (i.e. small ice particles, snowflakes, ice aggregates) in the latest stage of its lifetime, when a shallow WC appeared at lowers levels. Therefore, diabatic processes played a role in its WC development. This is in line with the microphysical characteristics detected within the WC region (i.e. within 100 km from the WC center) for other medicanes. Panegrossi et al. (2023) highlighted that all the six medicanes analyzed from 2014 are characterized by the presence of DC during the WC phase within 100 km from the WC center (in particular for Ianos and Zorbas, although it is weaker than during the early development phase), but in four out of six cases, including Qendresa, it is quite rare and weak. At the same time, the CTH showed values generally higher than 8–10 km, with maximum values up to 15 km registered for Medicane Ianos. The CTH values retrieved for both Helios and Juliette are generally lower than 8 km during their WC phases, with higher values (even if they reached just about 10 km) only in the outer bands a few hundred km far from the center. Furthermore, the DEEPSTORM-based CTH product highlights the absence of a closed cloud-free eye for Helios, while for Juliette it is visible when the WC is detected (on 1 March).

Previous works investigated the presence and the role of DC for different Mediterranean cyclones. Dafis et al. (2020) using a multispectral (i.e. combination of IR and MW data) analysis found that only a fraction of analyzed cyclones revealed the presence of DC within their centers. Lagouvardos et al. (2022) reported that Ianos (the strongest observed medicane so far) presented an intense DC activity within its center, highlighting different characteristics with respect to potential medicanes analyzed by Claud et al. (2010) and Miglietta et al. (2013). It is worth noting that the lack of ice and DC for Helios and their scarce presence in Juliette could be partially related to the winter season during which they occurred, which does not favor the development of strong vertical motions due to the cold temperatures at the surface.

In conclusion, although Helios and Juliette show, in the first phases of their lifetime, thermodynamic properties similar to other medicanes, with a development of an upper-level warm anomaly associated with stratospheric-air intrusion and its vertical alignment with the surface low. The mid−/low- troposphere WC development is mainly due to the seclusion of the warm air within the cyclone core, except for the latest phase in Juliette where the PMW analysis evidence a tropical transition with the occurrence of a WC due to diabatic heating. While for Helios the analysis evidences different microphysical properties compared to other medicanes, highlighting the absence of ice hydrometeors and DC within the WC region, for Juliette ice and DC are found in proximity of the cyclone center. For this reason, from an observational satellite-based perspective, Helios can not be classified as a tropical-like cyclone while Juliette exhibits some tropical-like cyclone features during its lifetime. A future development of the present work is the extension of the analysis to a list of potential medicanes (i.e., WC cyclones) going back to the beginning of the 2000's when the first AMSU-A measurements were collected. In addition, the present work is a contribution in the medicane definition activity within the EU COST Action MedCyclones (CA19109).

CRediT authorship contribution statement

Leo Pio D'Adderio: Conceptualization, Methodology, Software, Writing – original draft, Writing – review & editing. **Giulia Panegrossi:** Data curation, Supervision, Writing – original draft, Writing – review & editing. **Stavros Dafis:** Writing – original draft, Writing – review & editing. **Jean-Francois Rysman:** Software, Writing – review & editing. **Daniele Casella:** Investigation, Writing – review & editing. **Paolo Sanò:** Investigation, Writing – review & editing. **Alessandro Fuccello:** Software. **Mario Marcello Miglietta:** Writing – original draft, Writing – review & editing.

Declaration of Competing Interest

The authors declare that they have no known competing financial interests or personal relationships that could have appeared to influence the work reported in this paper.

Data availability

I have shared the link of publicly available data in the Attach File step

Acknowledgments

This research was supported by the EUMETSAT Satellite Application Facility for Hydrology and Water Management (H SAF) Fourth Continuous Development and Operation Phase (CDOP-4). This article was partially based upon work from COST Action CA19109 MedCyclones; European Network for Mediterranean Cyclones in weather and climate, supported by COST - European Cooperation in Science and Technology (www.cost.eu). The efforts from the NASA Precipitation Processing System (PPS) data archive is gratefully acknowledged for hosting and making the GPM GMI and AMSR2 products freely available. The National Center of Aerospace Meteorology and Climatology (CNMCA) of the Italian Air Force is gratefully acknowledged for providing the synoptic maps. The DEEPSTORM dataset is available through the French national center for Atmospheric data and services AERIS (www.aeris-data.fr). AMSU and ATMS data are provided by the NOAA CLASS facility www.avl.class.noaa.gov/ (last access 9 March 2023). The authors express their sincere gratitude to Derrick Herndon (CIMSS/SSEC Madison, WI USA) for the fruitful scientific discussions and interactions during this work.

References

Bentley, A.M., Metz, N.D., 2016. Tropical transition of an unnamed, high-latitude, tropical cyclone over the Eastern North Pacific. Mon. Weather Rev. 144, 713–736. https://doi.org/10.1175/MWR-D-15-0213.1.

Bentley, A.M., Bosart, L.F., Keyser, D., 2017. Upper-tropospheric precursors to the formation of subtropical cyclones that undergo tropical transition in the North Atlantic Basin. Mon. Weather Rev. 145, 503–520. https://doi.org/10.1175/MWR-D-16-0263.1.

Brueske, K.F., Velden, C.S., 2003. Satellite-based tropical cyclone intensity estimation using the NOAA-KLM series advanced microwave sounding unit (AMSU). Mon. Weather Rev. 131, 687–697. https://doi.org/10.1175/1520-0493(2003)131<0687:SBTCIE>2.0.CO;2.

Casella, D., do Amaral, L.M.C., Dietrich, S., Marra, A.C., Sanò, P., Panegrossi, G., 2017. The cloud dynamics and radiation database algorithm for AMSR2: exploitation of the GPM observational dataset for operational applications. IEEE J. Select. Topics Appl. Earth Observ. Remote Sens. 10, 3985–4001. https://doi.org/10.1109/JSTARS.2017.2713485.

Cecil, D.J., Chronis, T., 2018. Polarization-corrected temperatures for 10-, 19-, 37-, and 89-GHz passive microwave frequencies. J. Appl. Meteorol. Climatol. 57, 2249–2265. https://doi.org/10.1175/JAMC-D-18-0022.1.

Claud, C., Alhammoud, B., Funatsu, B.M., Chaboureau, J.-P., 2010. Mediterranean hurricanes: large-scale environment and convective and precipitating areas from satellite microwave observations. Nat. Hazards Earth Syst. Sci. 10, 2199–2213. https://doi.org/10.5194/nhess-10-2199-2010.

D'Adderio, L.P., Casella, D., Dietrich, S., Sanò, P., Panegrossi, G., 2022. GPM-CO observations of Medicane Ianos: Comparative analysis of precipitation structure between development and mature phase. Atmos. Res. 273, 106174 https://doi.org/10.1016/j.atmosres.2022.106174.

Dafis, S., Rysman, J., Claud, C., Flaounas, E., 2018. Remote sensing of deep convection within a tropical-like cyclone over the Mediterranean Sea. Atmos. Sci. Lett. 19 https://doi.org/10.1002/asl.823.

Dafis, S., Claud, C., Kotroni, V., Lagouvardos, K., Rysman, J., 2020. Insights into the convective evolution of Mediterranean tropical-like cyclones. Q.J.R. Meteorol. Soc. 146, 4147–4169. https://doi.org/10.1002/qj.3896.

Dowdy, A.J., Pepler, A., Di Luca, A., Cavicchia, L., Mills, G., Evans, J.P., Louis, S., McInnes, K.L., Walsh, K., 2019. Review of Australian east coast low pressure systems and associated extremes. Clim. Dyn. 53, 4887–4910. https://doi.org/10.1007/s00382-019-04836-8.

Draper, D.W., Newell, D.A., Wentz, F.J., Krimchansky, S., Skofronick-Jackson, G.M., 2015. The Global Precipitation Measurement (GPM) Microwave Imager (GMI): Instrument Overview and Early On-Orbit Performance. IEEE J. Select. Topics Appl. Earth Observ. Remote Sens. 8, 3452–3462. https://doi.org/10.1109/JSTARS.2015.2403303.

Emanuel, K., 2005. Genesis and maintenance of "Mediterranean hurricanes&quot. Adv. Geosci. 2, 217–220. https://doi.org/10.5194/adgeo-2-217-2005.

Evans, J.L., Braun, A., 2012. A Climatology of Subtropical Cyclones in the South Atlantic. J. Clim. 25, 7328–7340. https://doi.org/10.1175/JCLI-D-11-00212.1.

Evans, J.L., Guishard, M.P., 2009. Atlantic subtropical storms. Part I: Diagnostic criteria and composite analysis. Mon. Weather Rev. 137, 2065–2080. https://doi.org/10.1175/2009MWR2468.1.

Fita, L., Flaounas, E., 2018. Medicanes as subtropical cyclones: the December 2005 case from the perspective of surface pressure tendency diagnostics and atmospheric water budget. Q.J.R. Meteorol. Soc. 144, 1028–1044. https://doi.org/10.1002/qj.3273.

Flaounas, E., Gray, S.L., Teubler, F., 2021. A process-based anatomy of Mediterranean cyclones: from baroclinic lows to tropical-like systems. Weather Clim. Dynam. 2, 255–279. https://doi.org/10.5194/wcd-2-255-2021.

Flaounas, E., Davolio, S., Raveh-Rubin, S., Pantillon, F., Miglietta, M.M., Gaertner, M.A., Hatzaki, M., Homar, V., Khodayar, S., Korres, G., Kotroni, V., Kushta, J., Reale, M., Ricard, D., 2022. Mediterranean cyclones: current knowledge and open questions on dynamics, prediction, climatology and impacts. Weather Clim. Dynam. 3, 173–208. https://doi.org/10.5194/wcd-3-173-2022.

González-Alemán, J.J., Valero, F., Martín-León, F., Evans, J.L., 2015. Classification and synoptic analysis of subtropical cyclones within the Northeastern Atlantic Ocean*. J. Clim. 28, 3331–3352. https://doi.org/10.1175/JCLI-D-14-00276.1.

Hart, R.E., 2003. A cyclone phase space derived from thermal wind and thermal asymmetry. Mon. Weather Rev. 131, 585–616. https://doi.org/10.1175/1520-0493(2003)131<0585:ACPSDF>2.0.CO;2.

Hatzaki, M., Flaounas, E., Davolio, S., Pantillon, F., Patlakas, P., Raveh-Rubin, S., Hochman, A., Kushta, J., Khodayar, S., Dafis, S., Liberato, M.L.R., 2023. MedCyclones: working together toward understanding mediterranean cyclones. Bull. Am. Meteorol. Soc. 104, E480–E487. https://doi.org/10.1175/BAMS-D-22-0280.1.

Hong, G., Heygster, G., Miao, J., Kunzi, K., 2005. Detection of tropical deep convective clouds from AMSU-B water vapor channels measurements. J. Geophys. Res. 110 https://doi.org/10.1029/2004JD004949.

Hoskins, B.J., McIntyre, M.E., Robertson, A.W., 2007. On the use and significance of isentropic potential vorticity maps. Q.J.R. Meteorol. Soc. 111, 877–946. https://doi.org/10.1002/qj.49711147002.

Hou, A.Y., Kakar, R.K., Neeck, S., Azarbarzin, A.A., Kummerow, C.D., Kojima, M., Oki, R., Nakamura, K., Iguchi, T., 2014. The global precipitation measurement mission. Bull. Am. Meteorol. Soc. 95, 701–722. https://doi.org/10.1175/BAMS-D-13-00164.1.

Hourngir, D., Panegrossi, G., Casella, D., Sanò, P., D'Adderio, L.P., Liu, C., 2021. A 4-year climatological analysis based on GPM observations of deep convective events in the Mediterranean Region. Remote Sens. 13, 1685. https://doi.org/10.3390/rs13091685.

Kuo, Y.-H., Shapiro, M.A., Donall, E.G., 1991. The interaction between baroclinic and diabatic processes in a numerical simulation of a rapidly intensifying extratropical marine cyclone. Mon. Weather Rev. 119, 368–384. https://doi.org/10.1175/1520-0493(1991)119<0368:TIBBAD>2.0.CO;2.

Lagouvardos, K., Karagiannidis, A., Dafis, S., Kalimeris, A., Kotroni, V., 2022. Ianos—a Hurricane in the Mediterranean. Bull. Am. Meteorol. Soc. 103, E1621–E1636. https://doi.org/10.1175/BAMS-D-20-0274.1.

Loli, M., Kefalas, G., Dafis, S., Mitoulis, S.A., Schmidt, F., 2022. Bridge-specific flood risk assessment of transport networks using GIS and remotely sensed data. Sci. Total Environ. 850, 157976 https://doi.org/10.1016/j.scitotenv.2022.157976.

Marra, A.C., Federico, S., Montopoli, M., Avolio, E., Baldini, L., Casella, D., D'Adderio, L. P., Dietrich, S., Sanò, P., Torcasio, R.C., Panegrossi, G., 2019. The precipitation structure of the mediterranean tropical-like cyclone numa: analysis of GPM observations and numerical weather prediction model simulations. Remote Sens. 11, 1690. https://doi.org/10.3390/rs11141690.

Mazza, E., Ulbrich, U., Klein, R., 2017. The tropical transition of the October 1996 medicane in the Western Mediterranean Sea: a warm SECLUSION EVENT. Mon. Weather Rev. 145, 2575–2595. https://doi.org/10.1175/MWR-D-16-0474.1.

Menna, M., Martellucci, R., Reale, M., Cossarini, G., Salon, S., Notarstefano, G., Mauri, E., Poulain, P.-M., Gallo, A., Solidoro, C., 2023. A case study of impacts of an extreme weather system on the Mediterranean Sea circulation features: Medicane Apollo (2021). Sci. Rep. 13, 3870. https://doi.org/10.1038/s41598-023-29942-w.

Miglietta, M.M., Rotunno, R., 2019. Development mechanisms for Mediterranean tropical-like cyclones (medicanes). Q.J.R. Meteorol. Soc. 145, 1444–1460. https://doi.org/10.1002/qj.3503.

Miglietta, M.M., Laviola, S., Malvaldi, A., Conte, D., Levizzani, V., Price, C., 2013. Analysis of tropical-like cyclones over the Mediterranean Sea through a combined modeling and satellite approach: TLC ANALYSIS THROUGH a COMBINED APPROACH. Geophys. Res. Lett. 40, 2400–2405. https://doi.org/10.1002/grl.50432.

Nastos, P.T., Karavana Papadimou, K., Matsangouras, I.T., 2018. Mediterranean tropical-like cyclones: Impacts and composite daily means and anomalies of synoptic patterns. Atmos. Res. 208, 156–166. https://doi.org/10.1016/j.atmosres.2017.10.023.

Okuyama, A., Imaoka, K., 2015. Intercalibration of advanced microwave scanning radiometer-2 (AMSR2) brightness temperature. IEEE Trans. Geosci. Remote Sens. 53, 4568–4577. https://doi.org/10.1109/TGRS.2015.2402204.

Panegrossi, G., D'Adderio, L.P., Dafis, S., Rysman, J.-F., Casella, D., Dietrich, S., Sanò, P., 2023. Warm core and deep convection in medicanes: a passive microwave-based investigation. Remote Sens. 15, 2838. https://doi.org/10.3390/rs15112838.

Rysman, J.-F., Claud, C., Dafis, S., 2021. Global monitoring of deep convection using passive microwave observations. Atmos. Res. 247, 105244 https://doi.org/10.1016/j.atmosres.2020.105244.

Rysman, J.-F., Claud, C., Dafis, S., 2022. A machine learning algorithm for retrieving cloud top height with passive microwave radiometry. IEEE Geosci. Remote Sens. Lett. 19, 1–5. https://doi.org/10.1109/LGRS.2021.3081920.

Skofronick-Jackson, G., Petersen, W.A., Berg, W., Kidd, C., Stocker, E.F., Kirschbaum, D. B., Kakar, R., Braun, S.A., Huffman, G.J., Iguchi, T., Kirstetter, P.E., Kummerow, C., Meneghini, R., Oki, R., Olson, W.S., Takayabu, Y.N., Furukawa, K., Wilheit, T., 2017. The global precipitation measurement (GPM) mission for science and society. Bull. Am. Meteorol. Soc. 98, 1679–1695. https://doi.org/10.1175/BAMS-D-15-00306.1.

Velden, C.S., Herndon, D., 2020. A consensus approach for estimating tropical cyclone intensity from Meteorological Satellites: SATCON. Weather Forecast. 35, 1645–1662. https://doi.org/10.1175/WAF-D-20-0015.1.

Weng, F., Yang, H., Zou, X., 2013. On convertibility from antenna to sensor brightness temperature for ATMS. IEEE Geosci. Remote Sens. Lett. 10, 771–775. https://doi.org/10.1109/LGRS.2012.2223193.

Yan, B., Ahmad, K., 2021. Derivation and validation of sensor brightness temperatures for advanced microwave sounding unit-a instruments. IEEE Trans. Geosci. Remote Sens. 59, 404–414. https://doi.org/10.1109/TGRS.2020.2992270.

Zou, X., Weng, F., Zhang, B., Lin, L., Qin, Z., Tallapragada, V., 2013. Impacts of assimilation of ATMS data in HWRF on track and intensity forecasts of 2012 four landfall hurricanes. J. Geophys. Res. Atmos. 118 https://doi.org/10.1002/2013JD020405.